Applied Thermal Engineering 179 (2020) 115484

Contents lists available at ScienceDirect

Applied Thermal Engineering

journal homepage: www.elsevier.com/locate/apthermeng

Heat transfer performance and flow characteristics of solar air heaters with inclined trapezoidal vortex generators

Hui Xiao, Zhimin Dong, Zhichun Liu, Wei Liu*

School of Energy and Power Engineering, Huazhong University of Science and Technology, Wuhan 430074, PR China

HIGHLIGHTS

- The inclined trapezoidal vortex generator is proposed to form multi longitudinal swirls flow.
- The upwind aligned arrangement gives the most intense vortex strength.
- The range of Nu/Nu_0, f/f_0, and R3 are 1.24–3.71, 1.39–11.8, and 1.11–1.89, respectively.
- The energy and exergy efficiency are maximally enhanced by 24% and 31%, respectively.

GRAPHICAL ABSTRACT

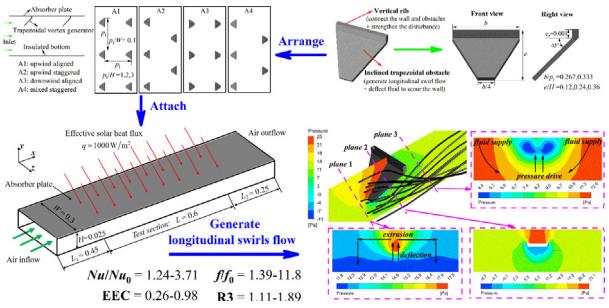

ARTICLE INFO

Keywords:
Solar air heater
Trapezoidal vortex generator
Thermal hydraulic performance
Energy conversion efficiency
Longitudinal swirls flow

ABSTRACT

Solar air heaters (SAHs) are widely used devices for solar energy utilization at low temperature. The low convective heat transfer performance limits the energy conversion efficiency. This paper was aimed at investigating the flow characteristics and heat transfer enhancement mechanism, thermal hydraulic performance, and energy conversion efficiency of the SAH fitted with novel inclined trapezoidal vortex generators (ITVGs). The heat transfer performance and flow characteristics of a simplified unit were obtained by numerical simulation. A pair of longitudinal swirls were found close to both sides of each ITVG and the shape of vortex was rectangular in the front view. In the range of this paper, the order of overall thermal hydraulic performance for four different arrangements was listed as: upwind aligned (A1) > mixed staggered (A4) > upwind staggered (A2) > downwind aligned (A3). Furthermore, the A1 arrangement was applied to study the thermal hydraulic performance by altering parameters b/p_t, e/H, and p_l/H with Reynolds number ranging from 6000 to 18,000. The range of Nu/Nu_0, f/f_0, EEC, and R3 were 1.24–3.71, 1.39–11.8, 0.26–0.98 and 1.11–1.89, respectively. On this basis, energy and exergy efficiency evaluations were carried out on the practical SAH integrated by sixteen basic units. The energy efficiency and exergy efficiency could be maximally enhanced by 24% and 31% compared with the smooth SAH, respectively.

1. Introduction

As a renewable alternative to conventional fossil energy, solar energy is clean and abundant. With regard to solar energy utilization, it would alleviate many challenging issues, such as energy security, climate change, unemployment, etc. [1,2]. Solar air heater (SAH) is a kind of flat plate heat exchangers that utilizes solar energy by absorbing solar radiation and transferring the heat from the absorber plate to the flowing air in the rectangular duct. It has inherent advantages of simplicity, easy maintenance, and low power consumption. SAHs are

* Corresponding author.
E-mail address: w_liu@hust.edu.cn (W. Liu).

https://doi.org/10.1016/j.applthermaleng.2020.115484
Received 3 January 2020; Received in revised form 1 April 2020; Accepted 14 May 2020
Available online 26 May 2020
1359-4311/

Nomenclature

A_p	area of absorber plate
b	width of the ITVG
c_p	specific heat capacity
D_h	hydraulic diameter
e	height of the ITVG
Ex	exergy
f	friction factor
h	heat transfer coefficient
H	heater height
I	turbulence intensity
I_T	incident solar radiation
k	turbulence kinetic energy
L	heater length
m	mass flow rate
N	number of transparent covers
Nu	Nusselt number
p	pressure
p_t	transverse pitch
p_l	longitudinal pitch
Pr	Prandtl number
q	effective heat flux
Q_s	incident solar energy
Q_u	air obtained energy
Re	Reynolds number
T	temperature
T_a	ambient temperature
T_f	fluid temperature
T_p	absorber plate temperature
T_s	apparent sun temperature
u_m	inlet mean velocity
u,v,w	velocity component
U_L	total heat loss heat coefficient
V_h	heat convection velocity
W	heater width
x,y,z	Cartesian coordinates

Greek symbols

β	synergy angle
γ	heater tilt angle
ε	turbulence dissipation rate
ε_g	emissivity of transparent cover
ε_p	emissivity of absorber plate
η_o	optical efficiency
η_1	energy efficiency
η_2	exergy efficiency
κ_{eff}	effective thermal conductivity
λ	thermal conductivity
μ	dynamic viscosity
μ_{eff}	effective dynamic viscosity
ρ	density
Φ	viscous heat dissipation
Ω	fluid domain
$\Omega_{x,abs,m}$	longitudinal vortex strength

devices for solar energy utilization at low to moderate temperature and widely applied in many fields associated with space heating [3], drying [4], desalination [5], and etc. [6]. However, the low heat transfer coefficient between the absorber plate and the flowing air causes high thermal resistance in the air side and high absorber plate temperature, which deteriorates the energy conversion efficiency of the SAH [7]. Thus, it is necessary to enhance the heat transfer performance in the duct of SAH so as to improve the energy and exergy efficiency. In addition, in order to facilitate the design of heat transfer enhancement component, it is of significant importance to explore the mechanism of flow characteristics and heat transfer enhancement in the enhanced SAH.

In general, heat transfer enhancement techniques can be classified into four major categories: (1) increasing heat transfer area; (2) generating secondary flow; (3) raising the turbulence intensity; and (4) thinning boundary layer thickness [8,9]. In the past few decades, researchers around the world have made continuous exploration and developed a variety of heat transfer enhancement components in the SAH, such as roughness [10], ribs [11], obstacles [12], baffles [13], fins [14], corrugations [15], and etc. [6,7].

Bhushan and Ranjit Singh [10] proposed artificial protrusions and experimentally analyzed the effect on heat transfer and friction in the SAH. They observed 3.8 and 2.2 times maximum enhancement in Nusselt number and friction factor. Alam and Kim [16] numerically investigated the thermal hydraulic performance of the SAH roughened with conical protrusions. They indicated that the secondary flow attributed by sharp edge of conical ribs disturbed sub-laminar layer and mixed the boundary flow and core flow. The maximum enhancement of Nusselt number and friction factor were 2.49 and 7.29 times, respectively. Yadav and Bhagoria [17] numerically investigated the effect of circular transverse wire ribs on the heat transfer and fluid flow in the SAH. A maximum overall performance of 1.65 was found with Reynolds number ranging from 3800 to 18,000. Kumar et al. [18] experimentally investigated the heat transfer and friction factor for the SAH equipped with S-shaped wire ribs. The maximum enhancement in Nusselt number, friction factor were 4.64 and 2.71, respectively. Sahu and Prasad [19] analytically investigated the exergetic performance of the SAH roughened with arc shaped wire ribs. Due to the heat transfer enhancement in convective heat transfer, the maximum exergy efficiency enhancement of 56% was found compared with the smooth absorber plate SAH. In order to generate more intense secondary flows, Promvonge [20] experimentally assessed the thermal performance of the v-baffled SAH. The maximum overall thermal enhancement factor was observed approximately at 1.87. Jin et al. [21] carried out a numerical study on the flow characteristics of the v-baffled SAH. Helical vortex flows were found to mix the colder mainstream and the warmer boundary flow. Sawhney et al. [22] proposed wavy delta winglets and experimentally obtained 3.2 and 10.9 times maximum enhancement in Nusselt number and friction factor compared with smooth duct. Chamoli et al. [23] proposed modified delta winglets and numerically found the enhanced times in Nusselt number, friction factor, and thermal enhancement factor were 2.11–4.71, 3.77–25.19, and 1.17–2.20, respectively. Akpinar and Kocyiğit [24] experimentally studied thermal performance of the SAH with several different types of obstacles. The results showed that the thermal efficiency was the highest with leaf obstacles. In order to further increase the disturbance on the fluid, some researchers proposed larger obstacles to generate significant flow disturbance associated with vortex flows, such as triangular obstacles [12], semi ellipse shaped obstacles [25], and spherical obstacles [26].

For the purpose of reducing flow resistance, Kumar et al. [27] experimentally investigated the effect of gapped v-shaped rib on thermal hydraulic performance with Reynolds number ranging from 2000 to 20,000. The performance reached the maximum when the relative gap distance equaled 0.69 and the relative gap width equaled 1.0. Ravi and Saini [28] proposed discrete staggered multi V shaped ribs for the SAH and experimentally found that the maximum enhancement of Nusselt number and friction factor were 9.64 and 8.53 times compared with smooth single pass SAH. Skullong et al. [29] proposed perforated rectangular and trapezoidal winglets to enhance heat transfer with

moderate flow resistance. The vortex flows were found and the best thermal performance was about 2.01 for the perforated trapezoidal winglet vortex generator. Promvonge and Skullong [30] punched hole in the rectangular wings and experimentally found that Nusselt number and friction factor were in the range of 3.89–5.52 times and 11.51–36.35 times over the flat-plate duct, respectively.

The above review indicates three points: firstly, this research is a hot topic at present and the heat transfer enhancement mechanism is still lack of adequate researches; secondly, generating secondary flow is an effective way to enhance heat transfer; thirdly, low flow resistance is the pursuit of researchers. As is known, random secondary flow may cause invalid disturbance which causes extra power consumption but has little effect on the heat transfer enhancement. Thus, it is necessary to design a heat transfer enhancement component based on an efficient secondary flow pattern and explore the corresponding heat transfer enhancement mechanism.

Multi longitudinal swirls flow was found as an optimal flow pattern in the circular tube by applying variation method combined with field synergy optimization [31] and exergy destruction principle [32]. Besides, Xiao et al. [33] found that multi longitudinal swirls flow was also a realizable optimal flow pattern in the SAH. Moreover, in the aspect of heat transfer enhancement analysis, Guo et al. [34] proposed field synergy principle and Liu et al. [35] extended this principle to multi-physical quantity synergy. In the view of field synergy principle, He and Tao [8] demonstrated that multi longitudinal swirls flow could increase the synergy performance so as to increase the thermal hydraulic performance. In addition, Zheng et al. [36] carried out a comprehensive review on the effect of multi longitudinal swirls flow on convective heat transfer enhancement. The multi longitudinal swirls flow was recommended to enhance the single phase convective heat transfer with the penalty of moderate flow resistance.

These previous results inspire the authors to enhance the heat transfer performance of the SAH by generating multi longitudinal swirls flow. When the fluid passes by an inclined structure, such as a slant rod [37], an awl-shaped slice [32], and a wedge shaped plate [9], a pair of longitudinal swirls can be observed. Besides, such discrete structures will not cause large flow resistance. In addition, the inclined trapezoidal structure could bring about lower flow resistance than the inclined rectangular structure as well as generate more intense longitudinal swirls flow than the inclined triangular structure. Thus, this paper proposed an inclined trapezoidal vortex generator (ITVG) to generate longitudinal swirls flow in the SAH, thereby enhancing the heat transfer performance in the air side to improve the solar energy utilization efficiency.

The motivation of this paper includes two points. On the one hand, this paper aims at enhancing the heat transfer performance of the SAH by generating multi longitudinal swirls flow. On this basis, the formation mechanism of multi longitudinal swirls flow will be revealed to facilitate the structure design in the SAH. On the other hand, this paper aims at investigating the thermal performance and flow characteristics of the SAH equipped with ITVGs. On this basis, the energy and exergy efficiency will be also investigated in the enhanced SAH. The main work of this paper is divided into three parts: firstly, the flow characteristics and heat transfer enhancement mechanism will be revealed with streamline visualization, heat convection velocity analysis, and arrangement analysis; secondly, the thermal hydraulic performance will be investigated with the variation of Reynolds number and configured parameters; thirdly, the enhancement in energy and exergy efficiency will be evaluated. This paper will be conducive to the design of heat transfer components and the improvement of solar energy utilization efficiency.

2. Theoretic efficiency analysis

As shown in Fig. 1, a conventional SAH consists of glass covers, absorber plates, and insulated bottom and edges. The absorber plate absorbs the solar radiation and thereby the plate temperature increases. The flowing air takes the heat away from the absorber plate when flowing through the duct. The energy efficiency and exergy efficiency of the SAH is closely related to the absorber plate temperature and the heat transfer coefficient between the absorber plate and air.

2.1. Energy efficiency analysis

The obtained energy Q_u of air is the difference between absorbed solar radiation and heat loss. It is expressed as

$$Q_u = A_p [\eta_o I_T - U_L (T_{p,m} - T_a)] \tag{1}$$

where A_p is the area of absorber plate, η_o is the optical efficiency, I_T is the incident solar radiation, U_L is the total heat loss coefficient, $T_{p,m}$ is the mean absorber plate temperature, and T_a is the ambient temperature.

The obtained energy Q_u can be also expressed as [38]

$$Q_u = A_p F_R [\eta_o I_T - U_L (T_{f,in} - T_a)] \tag{2}$$

where $T_{f,in}$ is the inlet temperature of working fluid.

The expression of F_R in Eq.(2) is written as

$$F_R = \frac{mc_p}{A_p U_L}\left[1 - \exp\left(-\frac{F' U_L A_p}{mc_p}\right)\right] \tag{3}$$

where

$$F' = \frac{Nu\lambda/D_h}{Nu\lambda/D_h + U_L} \tag{4}$$

The expression of U_L in Eq.(2) is written as

$$U_L = U_t + U_e + U_b \tag{5}$$

where U_t, U_e, and U_b are the top, edge, and bottom heat loss heat coefficient of the SAH, respectively.

The top heat loss U_t is the dominant part. When the mean plate temperature $T_{p,m}$ is between ambient temperature and 373 K, U_t can be evaluated by an empirical formula as

$$U_t = \left\{\frac{N}{\frac{C}{T_{p,m}}\left[\frac{T_{p,m} - T_a}{N + F}\right]^n} + \frac{1}{h_w}\right\}^{-1} + \frac{\sigma(T_{p,m} + T_a)(T_{p,m}^2 + T_a^2)}{\frac{1}{\varepsilon_p + 0.00591 N h_w} + \frac{2N + F - 1 + 0.133\varepsilon_p}{\varepsilon_g} - N} \tag{6}$$

where N is the number of transparent covers, ε_g is the emissivity of transparent cover, ε_p is emissivity of absorber plate, h_w is the wind heat transfer coefficient, and other parameters are expressed as

$$F = (1 + 0.089 h_w - 0.1166 h_w \varepsilon_p)(1 + 0.07866N)$$

$C = 520(1 - 0.000051\gamma^2)$, γ = heater tilt angle (°), $n = 0.430(1 - 100/T_{p,m})$

Through simultaneously solving Eqs. (1)–(6), Q_u can be obtained. The energy efficiency of the SAH can be expressed as

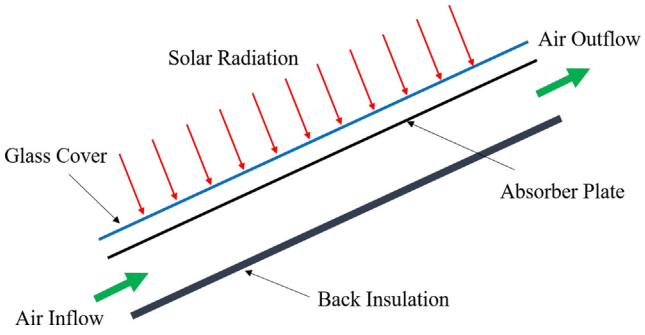

Fig. 1. The schematic of a conventional SAH.

$$\eta_1 = \frac{Q_u}{A_p I_T} \tag{7}$$

The *Nu* of the SAH affects the energy efficiency significantly. On the one hand, the increase of *Nu* can lead to the increase of F_R in Eq. (3). On the other hand, the increase of *Nu* can result in the decrease of mean absorber plate temperature $T_{p,m}$ and consequently cause the decrease of heat loss coefficient U_L. Thus, the increase of *Nu* consequently lead to the increase of Q_u, which improves the energy efficiency. Hence, the study of thermal hydraulic performance improvement is of great importance in the SAH.

2.2. Exergy efficiency analysis

The exergy balance equation is expressed as [14]

$$Ex_{heat} - Ex_{work} + Ex_{mass,in} - Ex_{mass,out} = Ex_d \tag{8}$$

On the basis of Eq.(8), the exergy balance equation can be written as

$$\left(1 - \frac{T_a}{T_s}\right) Q_s - m[\Delta h - T_a \Delta s] = Ex_d \tag{9}$$

where T_s is the apparent sun temperature which is approximately 4500 K [39].

The incident solar energy Q_s is expressed as

$$Q_s = I_T A_p \tag{10}$$

The enthalpy difference Δh and entropy difference Δs between the outlet and inlet are respectively expressed as

$$\Delta h = h_{out} - h_{in} = c_p (T_{f,out} - T_{f,in}) \tag{11}$$

$$\Delta s = s_{out} - s_{in} = c_p \ln \frac{T_{f,out}}{T_{f,in}} - R \ln \frac{p_{out}}{p_{in}} \tag{12}$$

Thus, the exergy efficiency can be expressed as [39]

$$\eta_2 = 1 - \frac{Ex_d}{[1 - T_a/T_s] Q_s} \tag{13}$$

In order to improve the exergy efficiency, the enthalpy difference Δh should be increased. The enthalpy difference is dependent on the obtained energy Q_u. Thus, the improvement of exergy efficiency demands the heat transfer improvement of the SAH. Hence, in the view of exergy efficiency, the study of thermal hydraulic performance improvement is of great importance in the SAH.

3. Model description

In order to investigate the heat transfer performance and flow characteristics of the air passageway of SAH, it is necessary to establish the corresponding simplified physical model. This paper considers a rectangular duct with one heated absorber plate and three insulated smooth wall, as shown in Fig. 2. The duct width (*W*) and height (*H*) are 0.3 m and 0.025 m, respectively. Thus, the ratio of width to height is 12 and the hydraulic diameter is 0.04615 m. These parameters can be also seen in other scientific papers [27,28,40]. The inlet length (L_1), test section length (*L*), and outlet length (L_2) are 0.45 m, 0.6 m, and 0.25 m, respectively. The inlet length and outlet length follow the suggestion of ASHARE Standard [41], and therefore the influence of inlet and outlet effect can be ignored. The uniform effective solar heat flux is assumed to be 1000 W/m^2 on the absorber plate for the convenience of simplicity. The same treatment can be also seen in other scientific papers [27,40].

In order to enhance the thermal hydraulic performance of the SAH, this paper attached new ITVGs to the absorber plate. The structure details of an ITVG are displayed in Fig. 3. The ITVG consists of a vertical rib and an inclined trapezoidal obstacle. The inclined trapezoidal obstacle is used to deflect fluid to scour the absorber plate and generate longitudinal swirls flow. The vertical rib is used to strengthen the disturbance and connect the absorber plate and the trapezoidal obstacle. The rib height (e_r) is 0.001 m and the tilt angle of the trapezoidal obstacle is 45°. As for the novelty of the ITVG, there are three points. Firstly, the present ITVGs are inclined and discrete so as to generate the multi longitudinal swirls flow. Secondly, the present ITVG has a low height and a narrow width, which is different from other obstacles. Thirdly, the present ITVG structure leads to low flow blockage.

As shown in Fig. 4, the arrangements of ITVGs are upwind aligned arrangement (A1), upwind staggered arrangement (A2), downwind aligned arrangement (A3), and mixed staggered arrangement (A4), respectively. The transverse pitch ratio p_t/W is fixed at 0.1. In this paper, the most efficient arrangement will be found firstly. The thermal hydraulic performance will be subsequently investigated by altering three configured parameters of b/p_t, e/H, and p_l/H with Reynolds number varying from 6000 to 18,000. The width ratio b/p_t is set to be 0.267 and 0.333. The height ratio e/H is 0.12, 0.24, and 0.36. And the longitudinal pitch ratio p_l/H is 1, 2, and 3.

4. Research methodology

In this paper, numerical simulations were carried out to investigate the flow characteristics and heat transfer enhancement mechanism of the SAH fitted with ITVGs. The research methodology details and results verifications are presented in this part.

4.1. Governing equations

As for the present three dimensional steady turbulent flow, the working fluid is assumed to be continuous and incompressible with constant thermal physical properties [13]. The Reynolds-averaged Navier-Stokes equations are employed to give the solution to this problem and the transport quantities are time averaged. In order to deal with the curvature flow, this paper applies the RNG *k*-ε turbulence model that has provided accurate results in other similar curvature flows [13,21,23,25,40]. Thus, the conservation equations can be written as follows:

Continuity equation:

$$\frac{\partial(\rho u_i)}{\partial x_i} = 0 \tag{14}$$

Momentum equation:

$$\frac{\partial}{\partial x_j}(\rho u_i u_j) = -\frac{\partial p}{\partial x_i} + \frac{\partial}{\partial x_j}\left[\mu_{eff}\left(\frac{\partial u_i}{\partial x_j} + \frac{\partial u_j}{\partial x_i}\right)\right] \tag{15}$$

Energy equation:

$$\frac{\partial}{\partial x_i}\left(\rho u_i c_p T - \kappa_{eff}\frac{\partial T}{\partial x_i}\right) = \Phi \tag{16}$$

RNG *k*-ε equations:

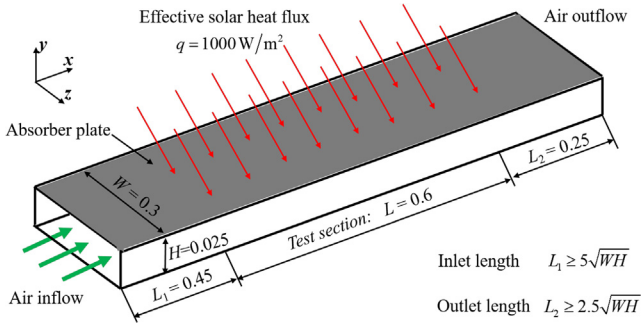

Fig. 2. The simplified physical model for the SAH.

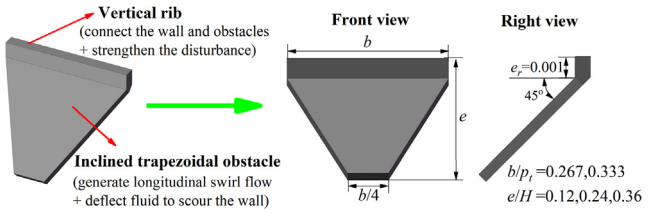

Fig. 3. Structure details of the ITVG.

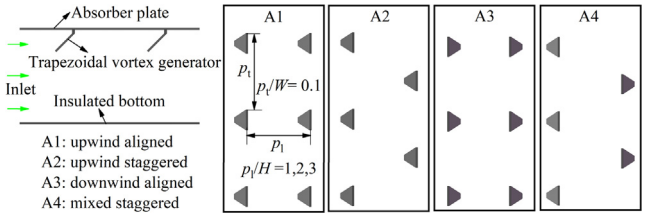

Fig. 4. Four arrangements of ITVGs in the SAH.

$$\frac{\partial}{\partial x_i}(\rho k u_i) = \frac{\partial}{\partial x_j}\left(\alpha_k \mu_{\text{eff}} \frac{\partial k}{\partial x_j}\right) + G_k - \rho\varepsilon \tag{17}$$

$$\frac{\partial}{\partial x_i}(\rho \varepsilon u_i) = \frac{\partial}{\partial x_j}\left(\alpha_\varepsilon \mu_{\text{eff}} \frac{\partial \varepsilon}{\partial x_j}\right) + C_{1\varepsilon}\frac{\varepsilon}{k}G_k - C_{2\varepsilon}\rho\frac{\varepsilon^2}{k} - R_\varepsilon \tag{18}$$

where $\mu_{\text{eff}} = \mu + \mu_t$, $\mu_t = \rho C_\mu k^2/\varepsilon$, $\kappa_{\text{eff}} = \lambda + \mu_t/\text{Pr}_t$, $\rho = 1.1773$ kg/m^3, $c_p = 1005$ J/(kg·K), $\lambda = 0.02642$ W/(m·K), $\text{Pr}_t = 0.85$, $C_\mu = 0.0845$, $C_{1\varepsilon} = 1.42$, $C_{2\varepsilon} = 1.68$, G_k represents the generation of turbulence kinetic energy due to the mean velocity gradients, the quantities α_k and α_ε are the inverse effective Prandtl numbers respectively for k and ε, and R_ε is a term for improving the accuracy of rapidly strained flows [42].

4.2. Boundary conditions

In order to save computational resources, a half width ($W/2$) of the computational domain is applied. A symmetry boundary condition is imposed at the symmetry plane of z = 0. The no slip velocity boundary is applied for all walls. A uniform effective heat flux of 1000 W/m^2 is imposed on the absorber plate and the adiabatic thermal boundary condition is applied for other walls. At the inlet, a uniform velocity profile is given with Re = 6000–18,000 and the temperature profile is uniform of 300 K. At the outlet, the pressure outlet boundary condition is specified. In addition, the turbulent intensity at the inlet and outlet can be estimated as [13]

$$I = 0.16\text{Re}^{-1/8} \tag{19}$$

4.3. Parameter definitions

In order to describe the thermal hydraulic characteristics, it is necessary to introduce some parameters.

Hydraulic diameter:

$$D_h = \frac{2WH}{W + H} \tag{20}$$

Reynolds number:

$$\text{Re} = \frac{\rho u_m D_h}{\mu} \tag{21}$$

Friction factor

$$f = \frac{\Delta p}{(L/D_h)\rho u_m^2/2} \tag{22}$$

Heat transfer coefficient:

$$h = \frac{q}{T_{p,m} - T_{f,m}} \tag{23}$$

Nusselt number:

$$Nu = \frac{hD_h}{\lambda} \tag{24}$$

The mean vortex strength of a specific cross section perpendicular to x direction can be described by the mass weighed absolute value of x-vorticity. It is defined as

$$\Omega_{x,abs,m} = \frac{\iint \rho u\, |\Omega_x|\, dS}{\iint \rho u dS} \tag{25}$$

where

$$\Omega_x = \frac{\partial w}{\partial y} - \frac{\partial v}{\partial z} \tag{26}$$

In addition, the evaluation criterion R3 [43] is an indicator of overall thermal hydraulic performance at an identical pump power consumption, which is defined as

$$\text{R3} = Nu/Nu_c \tag{27}$$

where Nu_c is the Nusselt number of the smooth tube at the equivalent Reynolds number Re_c. Given a constant pump power consumption, the equivalent Reynolds number Re_c can be calculated with

$$f_c\text{Re}_c^3 = f\text{Re}^3 \tag{28}$$

$$f_c = 0.34\text{Re}_c^{-0.25} \tag{29}$$

The relationship between Nu_c and Re_c is given as

$$Nu_c = 0.023\text{Re}_c^{0.8}\text{Pr}^{0.4} \tag{30}$$

In order to evaluate the resistance reduction performance, the criterion EEC is adopted and defined as

$$\text{EEC} = \frac{Nu/Nu_0}{f/f_0} \tag{31}$$

where Nu_0 and f_0 are Nusselt number and friction factor for the smooth duct at the identical Reynolds number, respectively.

4.4. Grid independence and computational method

The unstructured mesh is generated by commercial software ICEM 16.0. As depicted in Fig. 5, the mesh near duct walls and ITVGs is extremely dense, which guarantees $y^+ < 1$. The core flow region is fully filled with hexahedron mesh and the tetrahedron mesh is applied to

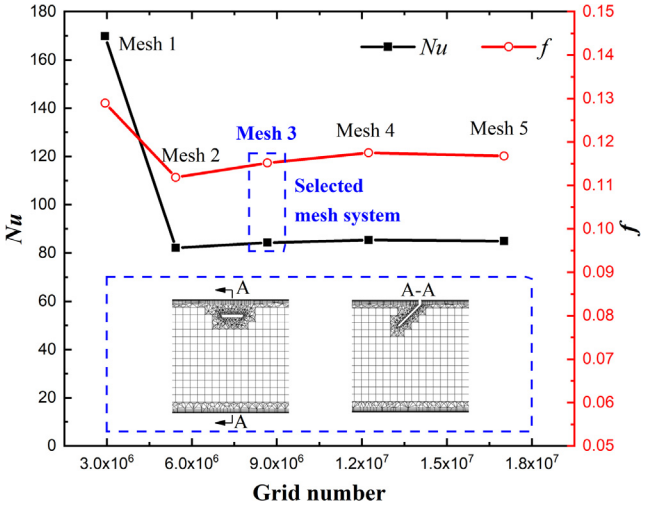

Fig. 5. Mesh details and grid independence test.

connect the hexahedron mesh and boundary layer mesh. In order to test the mesh independence, this paper generates five mesh systems from coarse to dense: Mesh 1 (2.9 million), Mesh 2 (5.4 million), Mesh 3 (8.7 million), Mesh 4 (12 million), and Mesh 5 (17 million). As shown in Fig. 5, when the grid number increases from 8.7 million to 17 million in the condition of $b/p_t = 0.267$, $e/H = 0.24$, $p_l/H = 2$, and $Re = 12{,}000$, the deviations of Nu and f are 0.8% and 1.3%, respectively. It indicates that Mesh 3 is adequately dense for this simulation, and therefore, Mesh 3 is adopted in this paper.

The simulation is carried out by commercial software FLUENT 16.0. The governing equations are discretized by finite volume method with second order scheme for pressure and second upwind scheme for other transport quantities. The SIMPLE algorithm is applied to handle the velocity and pressure coupling [44,45]. In addition, this paper applies the RNG k-ε turbulence model with enhanced wall treatment. When the relative residual is below 10^{-6} for energy equation and 10^{-4} for other equations or the residuals for all equations keep constant, the solution can be considered to be converged.

4.5. Results verifications

It is necessary to verify whether the effect of inlet and outlet is eliminated. The local Nu and f are displayed along the flow direction in Fig. 6 in the condition of $b/p_t = 0.267$, $e/H = 0.24$, $p_l/H = 2$, and $Re = 12{,}000$. As shown in Fig. 6, whether the Nusselt number or the friction factor are stable in the test section. It indicates that the location selection of the test section is reasonable.

The accuracy verifications are carried out by comparing with the empirical formulas of smooth duct and experimental results of enhanced duct, respectively. As for the smooth duct, the empirical formulas of Nusselt number and friction factor are expressed as [10,27,40]

Dittus-Boelter correlation:

$$Nu_0 = 0.023\mathrm{Re}^{0.8}\mathrm{Pr}^{0.4} \tag{32}$$

Modified Blasius correlation:

$$f_0 = 0.34\mathrm{Re}^{-0.25} \tag{33}$$

As displayed in Fig. 7(a), the Nu and f of present results agree well with the results of empirical formulas and the average deviations of Nu and f are less than 15% and 5%, respectively. It is similar in other scientific papers [26], which indicates that the simulation method and process are reasonable and reliable. As is known, the turbulence model selection is dependent on the flow pattern. It is of great significance to verify the present method with experimental results when similar flow pattern is formed. The v-shaped ribs, as depicted in Fig. 7(b), has been proved to form curvature flow [21] that is similar to the flow pattern in this paper. Thus, this paper carries out a verification with the experimental results of the enhanced duct fitted with v-shaped ribs provided by Promvonge [20]. As depicted in Fig. 7(b), the present numerical results agree well with the experimental results. Both of the present Nu and f are slightly less than the experimental results and the average deviations of Nu and f are 16.2% and 13.8%, respectively. In addition, this paper verifies the present method with the experimental results of delta wings [46] in the literature. The delta wing is visually similar to the present inclined trapezoidal vortex generator. The comparison is shown in Fig. 7(c) where the post processing of Nu is consistent with that in the literature [46]. The variation tendency of present numerical results is consistent with that of experimental results. The average deviations of Nu and f are 9.8% and 17.2%, respectively. Considering the experimental uncertainties in velocity, pressure drop, and temperature, the present results are reliable. Hence, the above research method can be employed for further study in the following.

5. Results and discussions

In this part, the flow characteristics and heat transfer enhancement mechanism will be revealed firstly. Furthermore, the effect of configured parameters b/p_t, e/H, and p_l/H on thermal hydraulic performance will be investigated. In addition, the energy and exergy efficiency will be evaluated by applying the obtained heat transfer performance.

5.1. Flow characteristics and heat transfer mechanism

5.1.1. Streamlines and temperature distributions

Fig. 8 shows the flow pattern in the condition of $b/p_t = 0.267$, $e/H = 0.24$, $p_l/H = 2$, and $Re = 12{,}000$ with A1 arrangement. As shown in Fig. 8(a), the front view of 3D streamlines indicates that multi longitudinal swirls flow is formed in the flow direction. There are two vortex cores symmetrically distributed on both sides of each ITVG. In the front view, the shape of vortex is rectangular. Fig. 8(b) shows the tangential velocity in the transverse plane of $x = 0.65$ m. It is shown that the transverse flow is regular and not disordered. Warm fluids near the absorber wall flow from the absorber plate to the bottom while cold fluids in the core flow region flow in the opposite direction. Ultimately, the fluid domain is fully disturbed.

Fig. 9 shows the pressure distribution around the ITVG so as to investigate the formation mechanism of the swirl flow. The working condition is $b/p_t = 0.267$, $e/H = 0.24$, $p_l/H = 2$, and $Re = 12{,}000$ with A1 arrangement. As depicted in the plane 1 of Fig. 9, in the front of ITVG, the fluid is deflected to scour the absorber wall. With fluid flowing forward, the static pressure is gradually increased so that the fluid is extruded to two sides of the ITVG where the static pressure is relative low. Thus, the fluid is accumulated between two transversely neighboring ITVGs and gradually flows from the absorber plate to the bottom, as the working fluid flows forward. In this way, multiple pairs of vortices are formed. As depicted in the plane 3 of Fig. 9, in the back of ITVG, the static pressure is the lowest, and therefore, the fluid below the ITVG is driven by pressure difference and flows from the bottom to the back of the ITVG. Simultaneously, the fluid between two transversely neighboring ITVGs flows away from the absorber plate to supply fluid for the bottom region. As a result, the multi longitudinal swirls flow is enhanced. Ultimately, the multi longitudinal swirls flow is formed when the fluid passes by the ITVGs periodically.

Fig. 10 displays the variation of local vortex strength, Nu, and f along the flow direction in the condition of $b/p_t = 0.267$, $e/H = 0.24$, $p_l/H = 2$, and $Re = 12{,}000$ with A1 arrangement. The longitudinal vortex strength reaches the maximum near the ITVGs and gradually weakens with the dissipation of vortex. Correspondingly, due to the fluid mixing that the longitudinal vortex brings about, Nu also reaches the maximum near the ITVGs and gradually decreases as the vortex strength weakens. The friction factor increases sharply in a narrow region around the ITVGs, but on the whole, it is at a low level due to the benefit of longitudinal swirls flow. Thus, it is worth noting that this kind of flow pattern can enhance heat transfer performance with

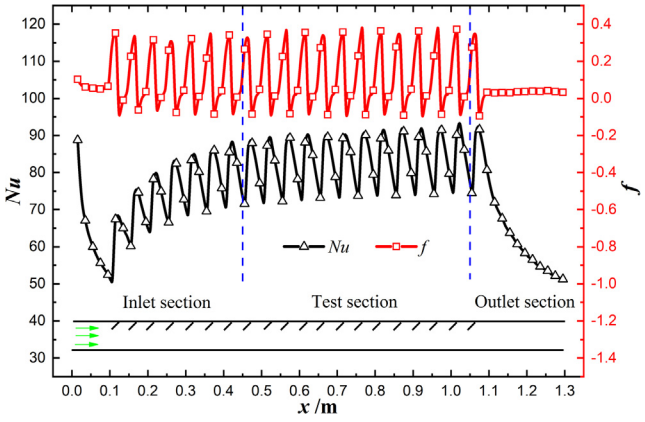

Fig. 6. Verification of the test section.

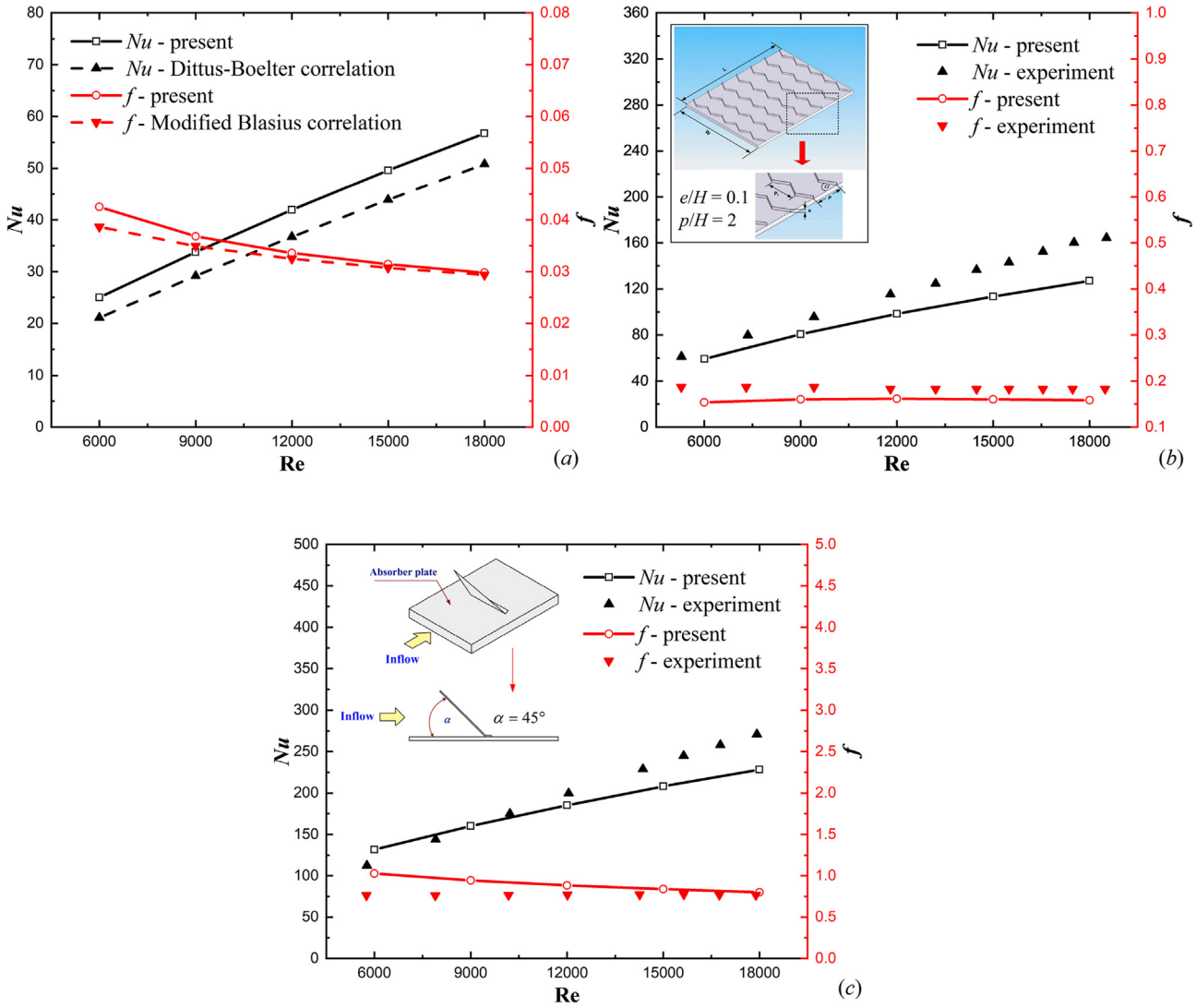

Fig. 7. Verifications with the (*a*) empirical formulas, (*b*) experimental results of v-shaped ribs and (*c*) experimental results of delta wings.

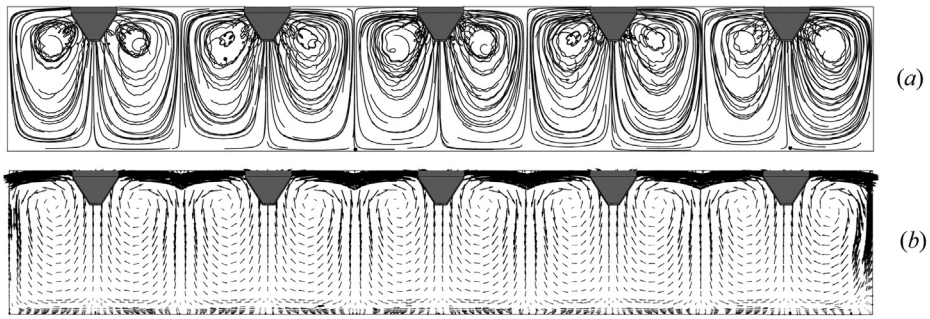

Fig. 8. Flow pattern: (*a*) front view of 3D streamlines and (*b*) tangential velocity in the transverse plane of $x = 0.65$ m.

moderate flow resistance.

Figs. 11 and 12 show the temperature distributions in the condition of $b/p_t = 0.267$, $e/H = 0.24$, $p_1/H = 2$, and $Re = 12{,}000$ with A1 arrangement. As shown in Fig. 11, the temperature distributions in the transverse plane of the enhanced duct is more uniform than that of smooth duct. It indicates a higher temperature gradient of the enhanced duct near the absorber plate, which is conducive to heat transfer between absorber plate and working fluid. Besides, the temperature field is an alternate distribution of warm fluid and cold fluid near the ITVGs, which is conducive to the heat transfer between fluid and fluid. In the present enhanced SAH, the cold fluid in the core flow is deflected to scour the heated absorber wall, thereby reducing the wall temperature. As shown in Fig. 12, the mean absorber plate temperature is decreased from 348 K to 327 K compared with the smooth duct. Hence, the mean temperature difference between absorber plate and working fluid is decreased correspondingly. As a result, the heat transfer performance is improved.

5.1.2. Heat convection velocity analysis

In order to further investigate the heat transfer enhancement

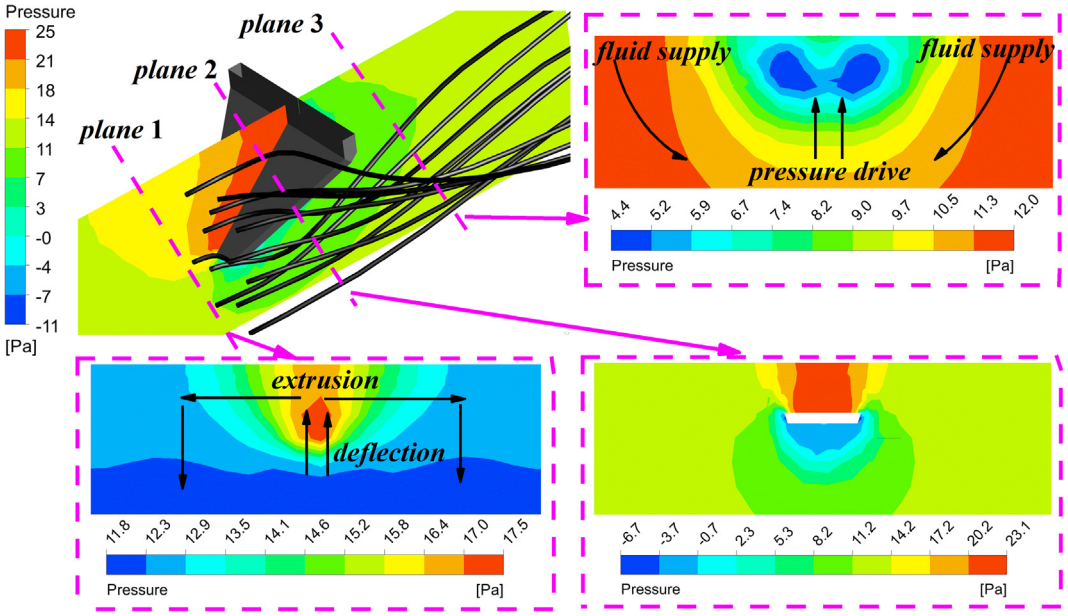

Fig. 9. Pressure distribution and swirl flow formation mechanism.

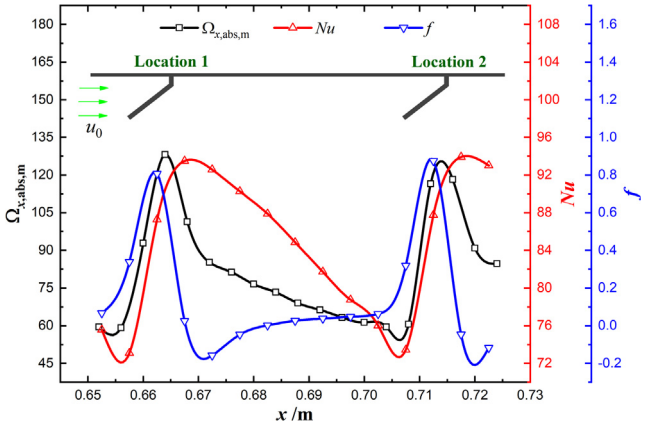

Fig. 10. Local vortex strength, *Nu*, and *f* along the flow direction.

mechanism in a new perspective of heat convection intensity, this paper carries out a heat convection velocity analysis in the condition of $b/p_t = 0.267$, $e/H = 0.24$, $p_1/H = 2$, and $Re = 12{,}000$ with A1 arrangement. Heat convection velocity [9] is the component of fluid velocity in the temperature gradient direction. It reflects the beneficial component of fluid velocity that contributes to heat convection. The component value is mathematically defined as

$$V_h = \frac{\mathbf{U}\cdot\nabla T}{|\nabla T|} = |\mathbf{U}|\cos\beta \tag{34}$$

where a larger absolute value of V_h stands for higher local heat convection intensity, whether the value is negative or positive.

On this basis, the mean heat convection velocity is defined as

$$V_{h,\mathrm{m}} = \frac{\iiint_{\Omega} |\mathbf{U}||\nabla T|\cos\beta dV}{\iiint_{\Omega} |\nabla T| dV} \tag{35}$$

As for the duct flow, integrating the energy equation Eq. in the test section, it yields

$$\iiint_{\Omega} \rho c_p \mathbf{U}\cdot\nabla T dV = \iint_{\text{in+out}} \vec{n}\cdot\kappa_{\text{eff}}\nabla T dS + \iint_{\text{wall}} \vec{n}\cdot\kappa_{\text{eff}}\nabla T dS + \iiint_{\Omega} \Phi dV \tag{36}$$

Neglecting the sum of heat conduction of inlet and outlet, it becomes

$$\iiint_{\Omega} \rho c_p \mathbf{U}\cdot\nabla T dV = \iint_{\text{wall}} \vec{n}\cdot\kappa_{\text{eff}}\nabla T dS + \iiint_{\Omega} \Phi dV \tag{37}$$

In the range of this research, the maximum ratio of viscous heat dissipation to absorbed heat from the absorber plate is 2.5% and the average ratio is 0.4%. Thus, the heat dissipation term can be neglected and it yields

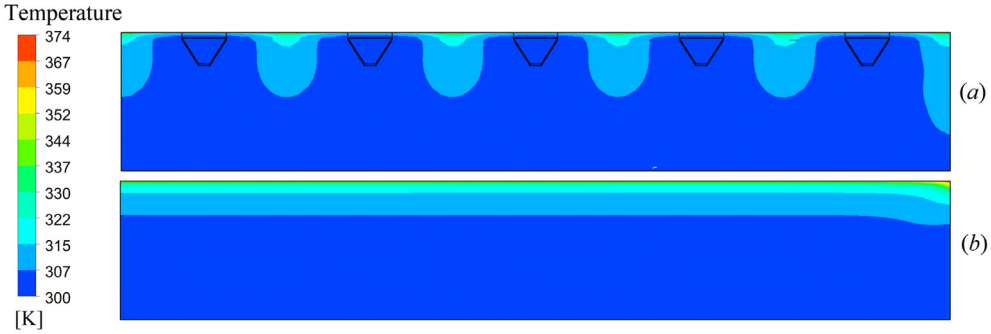

Fig. 11. Temperature distributions in the transverse plane of $x = 0.65$ m: (*a*) enhanced duct, (*b*) smooth duct.

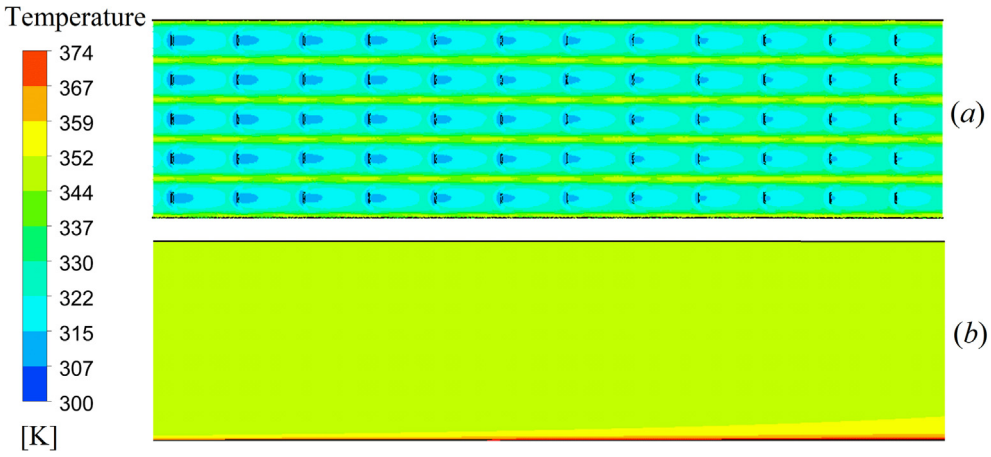

Fig. 12. Temperature distributions at the test section of absorber plate: (*a*) enhanced duct, (*b*) smooth duct.

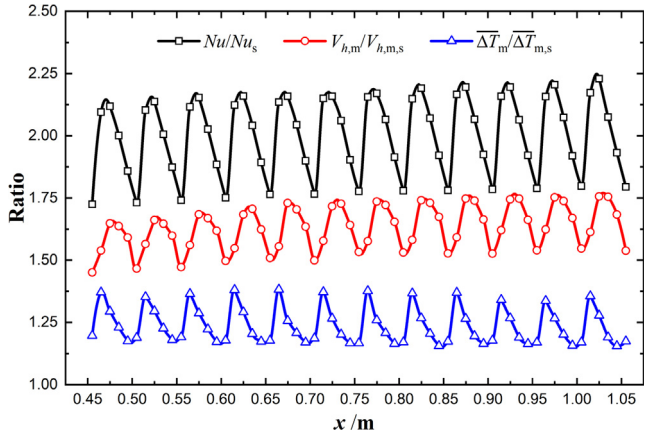

Fig. 13. The contribution of $V_{h,\mathrm{m}}/V_{h,\mathrm{m,s}}$ and $\Delta\bar{T}_{\mathrm{m}}/\Delta\bar{T}_{\mathrm{m,s}}$ to Nu/Nu_s

$$\iiint_{\Omega} \rho c_p \mathbf{U}\cdot\nabla T dV = \iint_{\mathrm{wall}} \vec{n}\cdot\kappa_{\mathrm{eff}}\nabla T dS = Q_{\mathrm{u}} \tag{38}$$

The absorbed heat can be also calculated by the Newtonian cooling formula as

$$Q_{\mathrm{u}} = hA_{\mathrm{p}}(T_{\mathrm{p,m}} - T_{\mathrm{f,m}}) \tag{39}$$

Comparing Eq. (38) with Eq. (39), the heat transfer coefficient is written as

$$h = \frac{\rho c_p V_{h,\mathrm{m}}}{hA_{\mathrm{p}}(T_{\mathrm{p,m}} - T_{\mathrm{f,m}})} \iiint_{\Omega} |\nabla T|\, dV \tag{40}$$

Thus, the Nusselt number can be expressed as

$$Nu = \rho c_p V_{h,\mathrm{m}} \frac{2}{\lambda A_{\mathrm{p}}} \iiint_{\Omega} |\bar{\nabla} T| dV \tag{41}$$

where the dimensionless temperature gradient is defined as

$$\bar{\nabla T} = \frac{\nabla T}{(T_{\mathrm{p,m}} - T_{\mathrm{f,m}})/\frac{D_{\mathrm{h}}}{2}} \tag{42}$$

The integration of dimensionless temperature gradient magnitude can be expressed as

$$\Delta\bar{T}_{\mathrm{m}} = \iiint_{\Omega} |\bar{\nabla} T| dV \tag{43}$$

Substituting Eq. (43) into Eq. (41), the Nusselt number can be also expressed as

$$Nu = \rho c_p V_{h,\mathrm{m}} \frac{2}{\lambda A_{\mathrm{p}}} \Delta\bar{T}_{\mathrm{m}} \tag{44}$$

Thus, the enhanced ratio of Nusselt number is expressed as

$$\frac{Nu}{Nu_s} = \frac{V_{h,\mathrm{m}}}{V_{h,\mathrm{m,s}}} \frac{\Delta\bar{T}_{\mathrm{m}}}{\Delta\bar{T}_{\mathrm{m,s}}} \tag{45}$$

where Nu_s, $V_{h,\mathrm{m,s}}$, and $\Delta\bar{T}_{\mathrm{m,s}}$ are taken from present simulation results of smooth duct at the same Reynolds number.

It indicates from Eq. that there are two available aspects for heat transfer enhancement. On the one hand, $V_{h,\mathrm{m}}$ should be increased in the view of changing velocity distribution. The available two methods are increasing the synergetic effect between velocity field and temperature field to increase $\cos\beta$ as well as deflecting the working fluid from the low temperature gradient region to the high temperature gradient region. On the other hand, $\Delta\bar{T}_{\mathrm{m}}$ should be increased in the view of changing temperature distribution. The available two methods are decreasing the mean temperature difference between absorber plate and

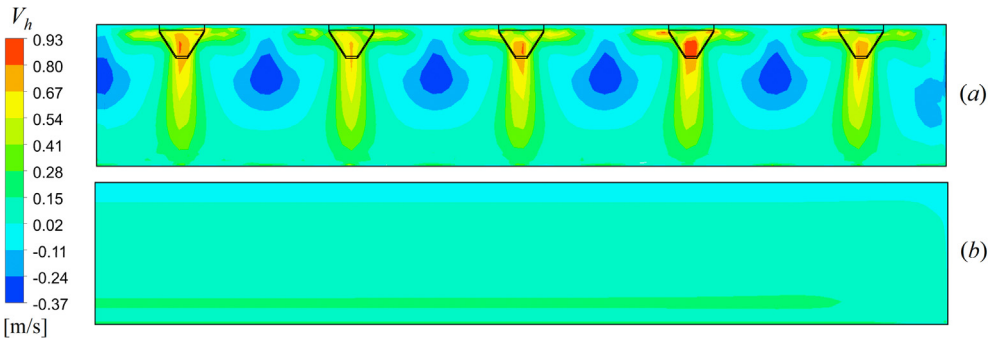

Fig. 14. The distribution of V_h in the transverse plane of $x = 0.65$ m.

working fluid as well as forming a temperature distribution with alternate warm fluid and cold fluid.

In order to investigate the heat transfer enhancement mechanism in the perspective of heat convection intensity, it is significant to investigate the contributions of $V_{h,\mathrm{m}}/V_{h,\mathrm{m,s}}$ and $\Delta\bar{T}_{\mathrm{m}}/\Delta\bar{T}_{\mathrm{m,s}}$ to Nu/Nu_s in the present SAH. Fig. 13 displays the variation of local Nu/Nu_{s}, $V_{h,\mathrm{m}}/V_{h,\mathrm{m,s}}$, and $\Delta\bar{T}_{\mathrm{m}}/\Delta\bar{T}_{\mathrm{m,s}}$ along the flow direction. The average Nu/Nu_{s}, $V_{h,\mathrm{m}}/V_{h,\mathrm{m,s}}$, and $\Delta\bar{T}_{\mathrm{m}}/\Delta\bar{T}_{\mathrm{m,s}}$ of the test section are 1.99, 1.62, and 1.23, respectively, which verifies the derived theoretical relation in Eq. (45). The $V_{h,\mathrm{m}}/V_{h,\mathrm{m,s}}$, which represents the enhancement of heat convection intensity, is the dominating reason of heat transfer enhancement. It indicates that the increase of $\cos\beta$ and fluid deflection in the fluid domain is of great significance for heat transfer enhancement. The $\Delta\bar{T}_{\mathrm{m}}/\Delta\bar{T}_{\mathrm{m,s}}$ also contributes to heat transfer enhancement. When the working fluid passes by the ITVG, the $\Delta\bar{T}_{\mathrm{m}}$ is increased sharply to the maximum due to the combined effects of local absorber plate temperature decrease and fluid mixing. Subsequently, while the heat convection intensity increases to the maximum, the $\Delta\bar{T}_{\mathrm{m}}$ decreases due to the decrease of the temperature gradient magnitude in the fluid domain. That is the reason that the peak value of $\Delta\bar{T}_{\mathrm{m}}/\Delta\bar{T}_{\mathrm{m,s}}$ comes prior to that of $V_{h,\mathrm{m}}/V_{h,\mathrm{m,s}}$. Both of $V_{h,\mathrm{m}}$ and $\Delta\bar{T}_{\mathrm{m}}$ contribute to the heat transfer enhancement and the following investigation lies in the enhancement mechanism of $V_{h,\mathrm{m}}$ and $\Delta\bar{T}_{\mathrm{m}}$, respectively.

It is necessary to compare the V_h and $|\bar{\nabla}T|$ of enhanced duct with that of smooth duct. Figs. 14 and 15 display the distributions of V_h and $|\bar{\nabla}T|$ in the transverse plane of $x = 0.65$ m, respectively. As depicted in Fig. 14, the local distribution of V_h is changed and the local absolute value of V_h is increased at most places. It indicates that the local heat convection is strengthened at most places. Though negative value of V_h appears, the region where the V_h is positive dominates the cross section, which leads to a positive value of $V_{h,\mathrm{m}}$. More importantly, in the near absorber plate region where the temperature gradient is relatively high, the V_h is increased and positive, which is the main reason for the increase of $V_{h,\mathrm{m}}$. As depicted in Fig. 15, the temperature gradient near the absorber plate is dramatically increased in the enhanced duct, which leads to the increase of $\Delta\bar{T}_{\mathrm{m}}$. As a result, with the increase of $V_{h,\mathrm{m}}$ and $\Delta\bar{T}_{\mathrm{m}}$, the heat transfer performance is improved.

5.1.3. Arrangements analysis

Arrangements always affect the flow pattern. It is necessary to investigate the flow characteristics and heat transfer performance with different arrangements. In this part, this paper compares the streamlines, the strength of longitudinal vortex, the temperature distributions, and the corresponding thermal hydraulic performance for different arrangements in the condition of $b/p_t = 0.267$, $e/H = 0.24$, $p_1/H = 1$, and $Re = 12{,}000$. In this way, the most excellent arrangement will be selected for subsequent research.

Fig. 16 displays the streamlines for four different arrangements. The streamlines are bent and the longitudinal swirls flow is formed no matter what arrangement is. When the arrangement is chosen as A1, A2, and A4, the streamlines are bent strongly when passing by the first row of ITVGs. When the arrangement is chosen as A3, the streamlines are bent slightly. The above comparison indicates that the upwind arranged ITVG can disturb fluid more drastically than the downwind arranged one. The reason can be explained as follows. The mass flow rate in the core flow region is much higher than that in the boundary flow region. The upwind arranged ITVG deflects the fluid from the core flow region to the boundary flow region. Compared with the mass flow rate in the boundary region, the deflected fluid mass flow rate is relatively high, which drastically changes the velocity in the boundary layer region. However, the downwind arranged ITVG deflects the fluid from the boundary flow region to the core flow region. Compared with the mass flow rate in the core region, the deflected fluid mass flow rate is relatively low, which slightly changes the velocity in the boundary and core region. Thus, the upwind arrangement is superior to the downwind arrangement in the aspect of disturbing fluid.

In order to compare the fluid disturbance strength and longitudinal vortex strength in a quantitative way, Fig. 17 shows the variations of $u_{yz,\mathrm{m}}/u_{\mathrm{m}}$ and $\Omega_{x,\mathrm{abs,m}}$ along the flow direction. The $u_{yz,\mathrm{m}}/u_{\mathrm{m}}$ is the ratio of average tangential velocity to the inlet velocity, which represents the fluid disturbance strength. The $\Omega_{x,\mathrm{abs,m}}$ denotes the average absolute value of x-vorticity, which represents the longitudinal vortex strength. As depicted in Fig. 17, the variation of $u_{yz,\mathrm{m}}/u_{\mathrm{m}}$ is similar to that of $\Omega_{x,\mathrm{abs,m}}$. In addition, when the arrangement is chosen as A2, the longitudinal swirl flow is crushed by the ITVGs in second row, which indicates that the A2 arrangement is inferior to the A1 arrangement. When the arrangement is chosen as A4, the longitudinal swirl flow is slightly strengthened by the ITVGs in second row. The disturbance caused by the second row is less intense than that caused by the first row, which indicates the A4 arrangement is also inferior to the A1 arrangement. Furthermore, the $u_{yz,\mathrm{m}}/u_{\mathrm{m}}$ and $\Omega_{x,\mathrm{abs,m}}$ of A1 arrangement are both larger than those of A2, A3, and A4 arrangements. It demonstrates that the A1 arrangement is superior to other three arrangements in the aspect of fluid disturbance and vortex strength.

High efficiency of the SAH demands for low absorber plate temperature. The absorber plate temperature is closely related to the arrangements. Fig. 18 displays the temperature distributions of the absorber plates for four different arrangements. The more effective the heat transfer enhancement structure is, the lower the absorber wall temperature is. As depicted in Fig. 18, the A1 arrangement leads to the lowest average and maximum temperature of the absorber plate. The order of the average absorber plate temperature value is listed as:

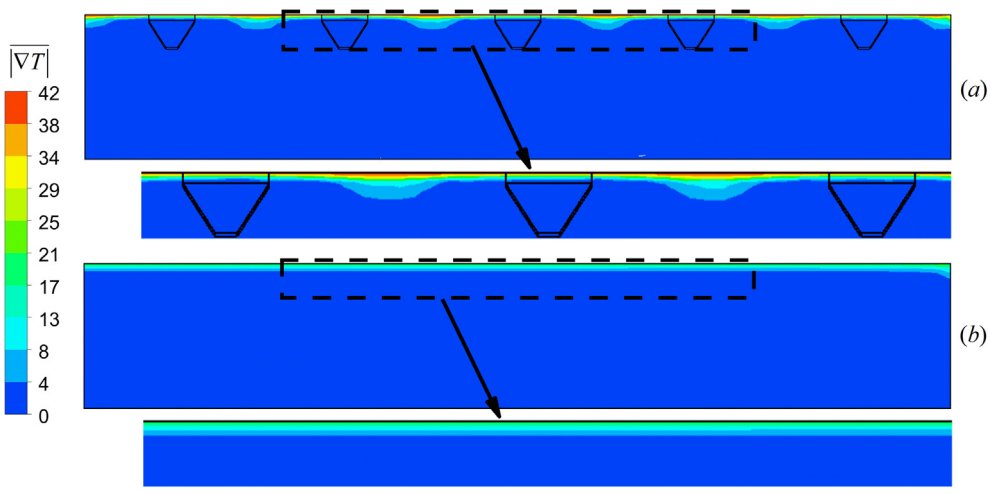

Fig. 15. The distribution of $|\bar{\nabla}T|$ in the transverse plane of $x = 0.65$ m.

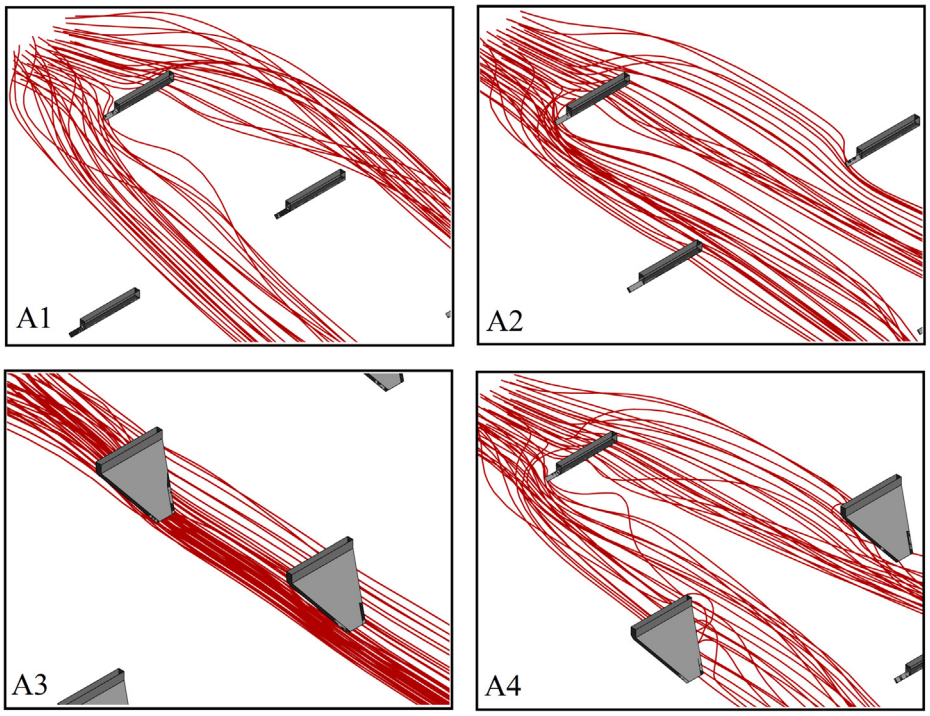

Fig. 16. Streamlines for four different arrangements in the condition of $b/p_t = 0.267$, $e/H = 0.24$, $p_1/H = 1$, and $Re = 12{,}000$.

A1 < A4 < A2 < A3. It demonstrates that the fluid disturbance in A1 arrangement is effective and conducive to the decrease of absorber plate temperature. Fig. 19 shows the variations of Nu/Nu_0, f/f_0, R3, and EEC for four different arrangements. It can be seen from Fig. 19(*a*) and (*b*) that both of the Nu/Nu_0 and f/f_0 in A1 arrangement are the highest compared with other arrangements. Besides, Fig. 19(*c*) shows that the EEC of all cases are near 0.5, which indicates that the flow resistance performance are similar for the four arrangements. In addition, as depicted in Fig. 19(*d*), the overall thermal hydraulic performance of A1 arrangement is also the highest.

Thus, the A1 arrangement is considered to be the best arrangement and chosen for the subsequent research.

5.2. Thermal hydraulic performance

In this part, the A1 arrangement is chosen for researching the thermal hydraulic performance of the SAH fitted with ITVGs in the variation condition of $b/p_t = 0.267,0.333$, $e/H = 0.12,0.24,0.36$, and $p_1/H = 1,2,3$.

In the above discussions, it demonstrates that the thermal hydraulic performance is closely related to the longitudinal vortex strength. In order to investigate the effect of parameters, it is necessary to display the variation of longitudinal vortex strength with the variation of parameters p_1/H, b/p_t and e/H. As depicted in Fig. 20(a), the decrease of longitudinal pitch leads to the increase of vortex strength. Besides, as depicted in Fig. 20(b), the longitudinal vortex strength is sensitive to the parameter e/H and the e/H should be increased to disturb the core flow for the purpose of guaranteeing intense longitudinal vortex. In addition, it presents that the increase of b/p_t also leads to the increase of longitudinal vortex strength, especially with a large e/H.

The indicators of thermal hydraulic performance are chosen as Nu/Nu_0, f/f_0, EEC, and R3. Figs. 21 and 22 display the variations of these indicators. In the condition of identical Reynolds number, both Nu/Nu_0 and f/f_0 are generally increased with the increase of e/H and the decrease of p_1/H. The Nu/Nu_0 and f/f_0 of $b/p_t = 0.333$ is generally slightly larger than those of $b/p_t = 0.267$ when all else held identical. The reason is that wider ITVGs can deflect more fluid so as to form more intense longitudinal vortex. These regularities are similar to those of longitudinal vortex strength. With the increase of Reynolds number, f/f_0 is always increased while Nu/Nu_0 may decrease. The reason is that

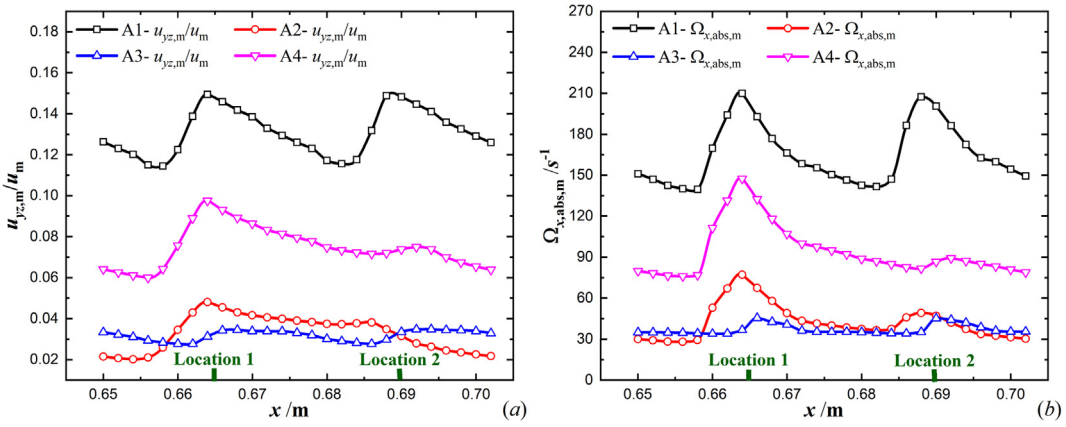

Fig. 17. (*a*) $u_{yz,m}/u_m$ and (*b*) $\Omega_{x,abs,m}$ for four different arrangements in the condition of $b/p_t = 0.267$, $e/H = 0.24$, $p_1/H = 1$, and $Re = 12{,}000$.

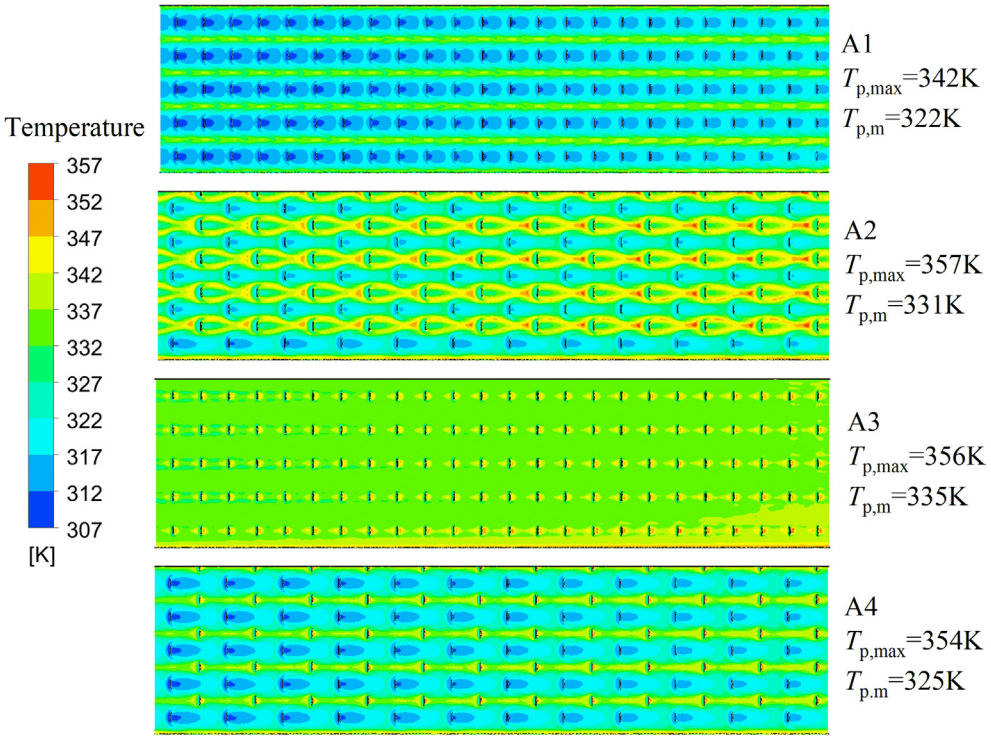

Fig. 18. Temperature distributions of the absorber plates for four different arrangements in the condition of b/p_t = 0.267, e/H = 0.24, p_1/H = 1, and Re = 12,000.

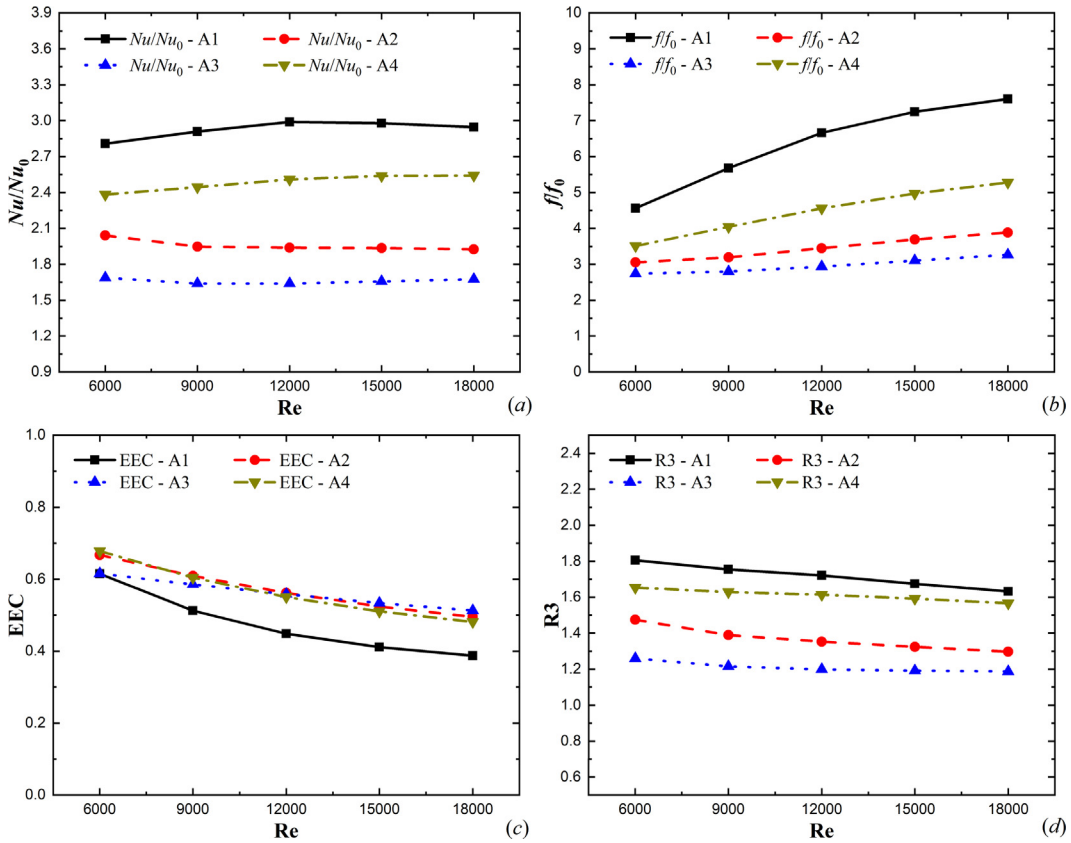

Fig. 19. (*a*) Nu/Nu_0, (*b*) f/f_0, (*c*) EEC, and (*d*) R3 for four different arrangements

the *Nu* of the smooth duct is also considerably large when Reynolds number is high. There is one detail worth noting. As shown in Fig. 22(a), Nu/Nu_0 decreases with e/H increasing from 0.24 to 0.36 when Reynolds number exceeds 15,000 in the condition of b/p_t = 0.333, p_1/H = 1. It owes to the unwanted backflow in the back of ITVGs, which suppresses the formation of longitudinal swirl flow. Thus, in order to avoid the backflow, it is recommended in this paper that b/p_t is below 0.333 and that e/H is below 0.36. In addition, due to the

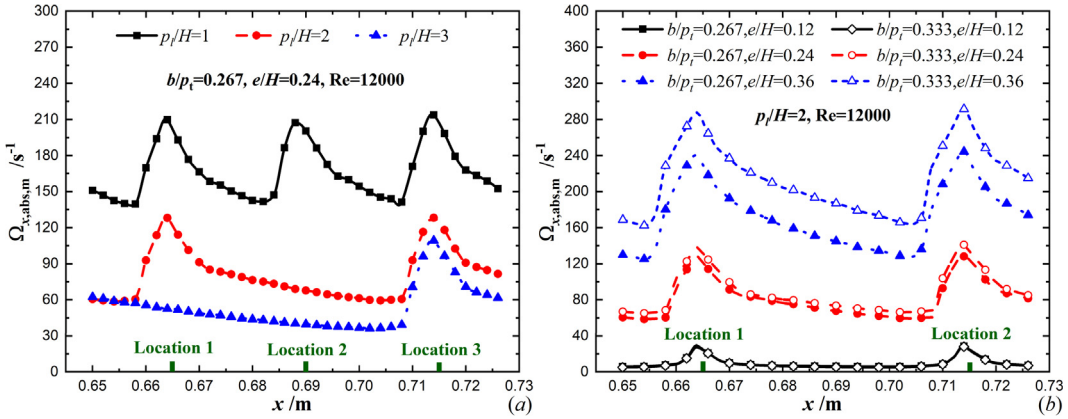

Fig. 20. The effect of configured parameters on longitudinal vortex strength: (*a*) p_1/H, (*b*) b/p_t and e/H.

demand of moderate flow resistance, it is dispensable to decrease p_1/H below 1.

To sum up, the range of Nu/Nu_0 and f/f_0 are 1.24–3.71 and 1.39–11.8, respectively. The range of EEC and R3 are 0.26–0.98 and 1.11–1.89, respectively. The overall performance criterion R3 is comparatively better in the condition of $e/H = 0.24$ and $p_1/H = 1$. Besides, the criterion EEC is larger when b/p_t is equal to 0.267, which indicates that the flow resistance reduction performance is better. Thus, this paper recommends the combined parameters of $p_1/H = 1$, $e/H = 0.24$, and $b/p_t = 0.267$.

5.3. Energy and exergy efficiency evaluation

Through the above investigations, the thermal hydraulic performance of a basic unit is obtained. Generally, the practical SAH is an integration of several such units. It is interesting to explore the effect of ITVGs on thermal performance and power consumption of the practical SAH. The power consumption is dependent on the friction factor, while the energy and exergy efficiency is dependent on the Nusselt number of the duct.

Refer to the Ref. [38], the adopted practical SAH is integrated with sixteen identical units and the size is of 0.025 m× 1.2 m× 4 m, as depicted in Fig. 23. The tilt angle is 45° and one glass cover is used. The optical efficiency is 0.82 and the emissivity is 0.1 and 0.88 for the

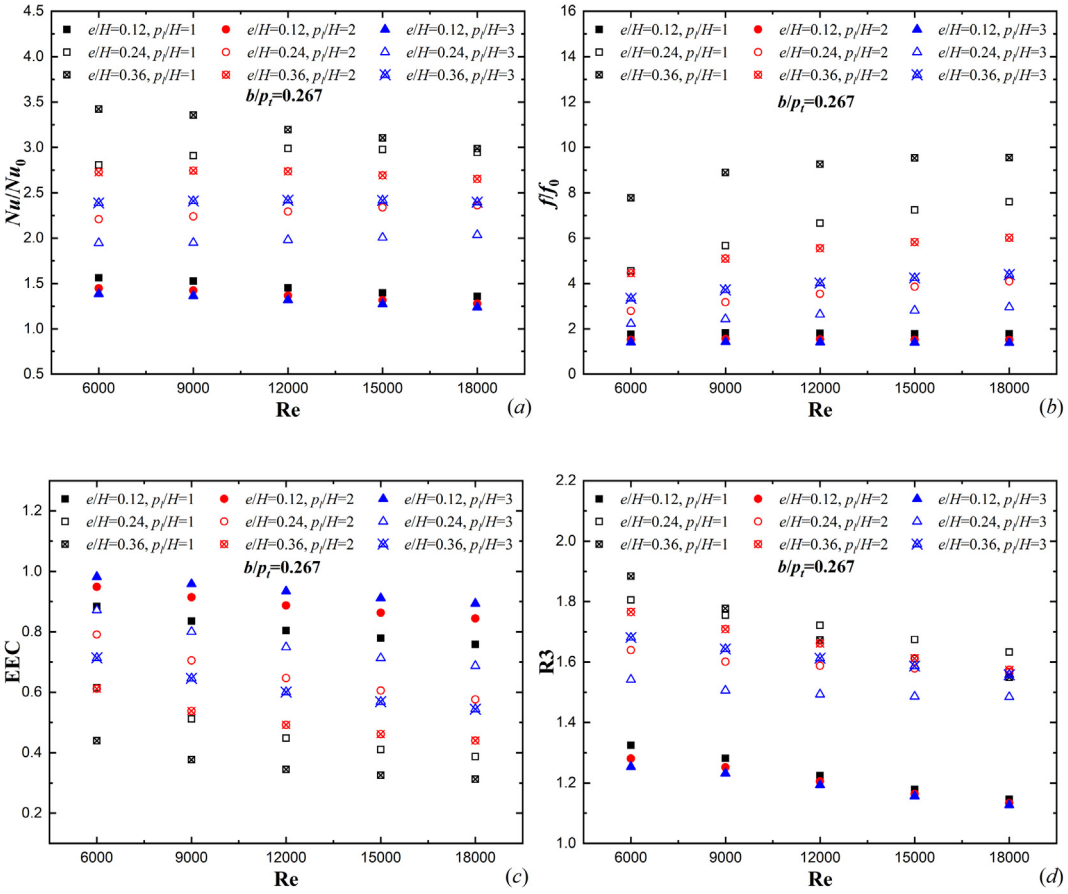

Fig. 21. The variation of thermal hydraulic performance with $b/p_t = 0.267$: (*a*) Nu/Nu_0, (*b*) f/f_0, (*c*) EEC, and (*d*) R3.

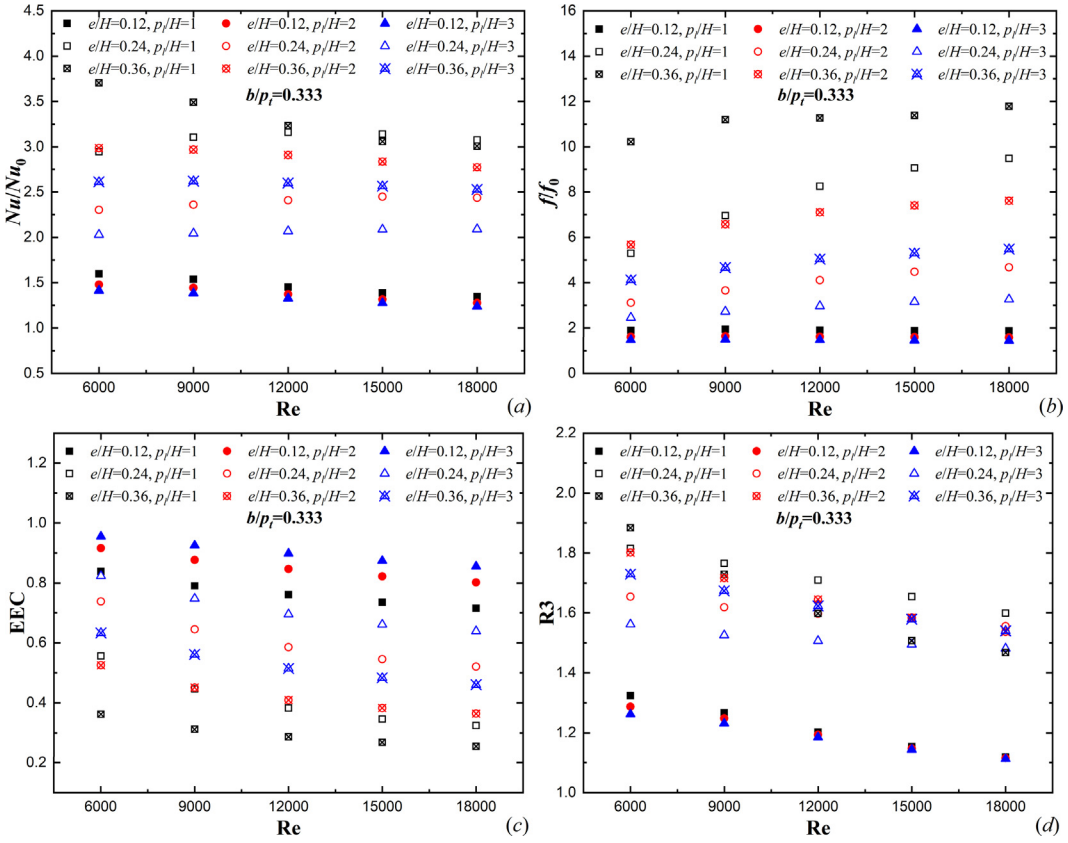

Fig. 22. The variation of thermal hydraulic performance with $b/p_t = 0.333$: (*a*) Nu/Nu_0, (*b*) f/f_0, (*c*) EEC, and (*d*) R3.

absorber plate and glass cover, respectively. The ambient temperature is 273 K and the duct inlet air temperature is 303 K. The wind heat transfer coefficient is 10W/(m²·K) and the sum of back and edge loss coefficients is 1W/(m²·K). The Reynolds number ranges from 6000 to 18,000 and the corresponding mass flow rate is 0.072–0.216kg/s. The thermal hydraulic performance of the duct is taken from the above investigations. Subsequently, the energy efficiency and exergy efficiency can be evaluated by Eq. (7) and Eq. (13).

Fig. 24 displays the variations of energy efficiency with the Reynolds number. The energy efficiency increases as the Reynolds number increases. Besides, the energy efficiency is increased with the increase of *Nu*. In the range of this research, the absolute value of energy efficiency can be maximally enhanced by 10.7%. The increased part is approximately 24% of the energy efficiency of smooth SAH at identical Reynolds number. Furthermore, when e/H is beyond 0.24 and p/H is below 2 (or Nu/Nu_0 approximately exceeds 2.5), the increase of heat transfer performance only leads to tiny improvement of energy efficiency. Fig. 25 displays the variations of exergy efficiency with the Reynolds number. In the condition of identical Reynolds number, the exergy efficiency is increased with the increase of *Nu* and the absolute value can be maximally increased by 2.1%. The increased part is approximately 31% of the exergy efficiency of the corresponding smooth SAH. Similar to the energy efficiency, when Nu/Nu_0 is beyond 2.5, the effect of Nu/Nu_0 on the exergy efficiency is also not obvious. With the increase of Reynolds number, the exergy efficiency of the smooth SAH increases while that of enhanced SAH generally decreases. Thus, in the range of this research, the exergy destruction is slightly decreased in the smooth SAH while it is increased in the enhanced SAH with the increase of Reynolds number. Fig. 26 displays the variations of power consumption with the Reynolds number. It indicates that the increased power consumption is not large.

5.4. Comparisons

The recommended configured parameters of $p_1/H = 1$, $e/H = 0.24$, and $b/p_t = 0.267$ is picked out for the comparison with other previous works. The typical heat transfer components are chosen as conical protrusion [16], v shaped baffle [20], wavy delta winglet [22], perforated trapezoidal winglet [29], and punched rectangular wing [30]. As depicted in Fig. 27, the enhancement in Nusselt number of present

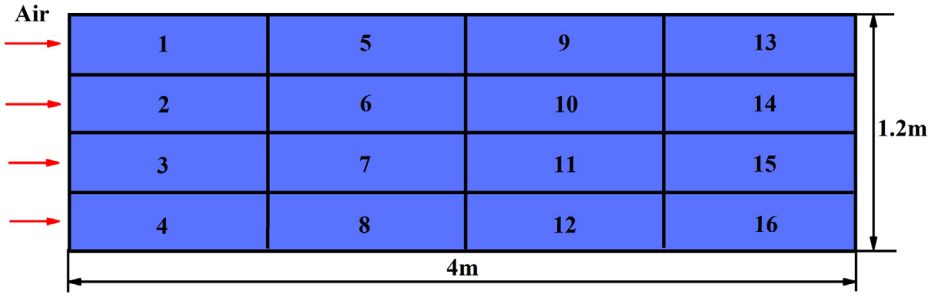

Fig. 23. The integration of a practical SAH.

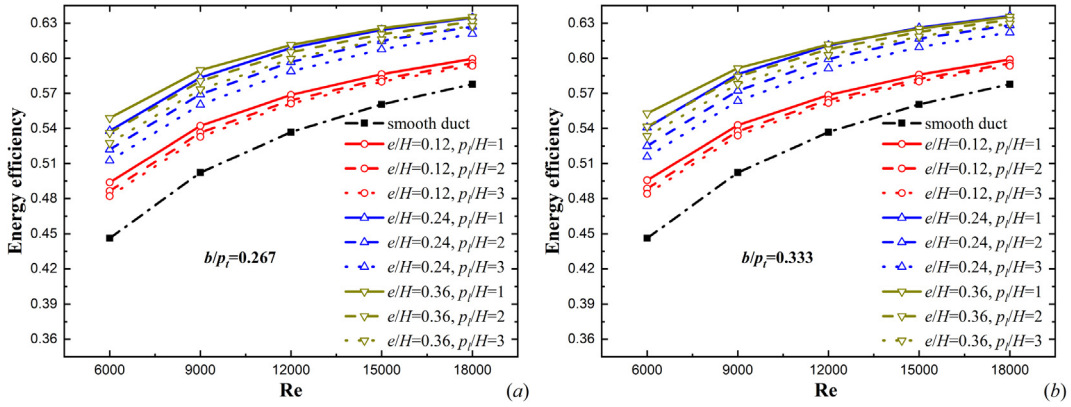

Fig. 24. The variations of energy efficiency: (*a*) $b/p_t = 0.267$, (*b*) $b/p_t = 0.333$.

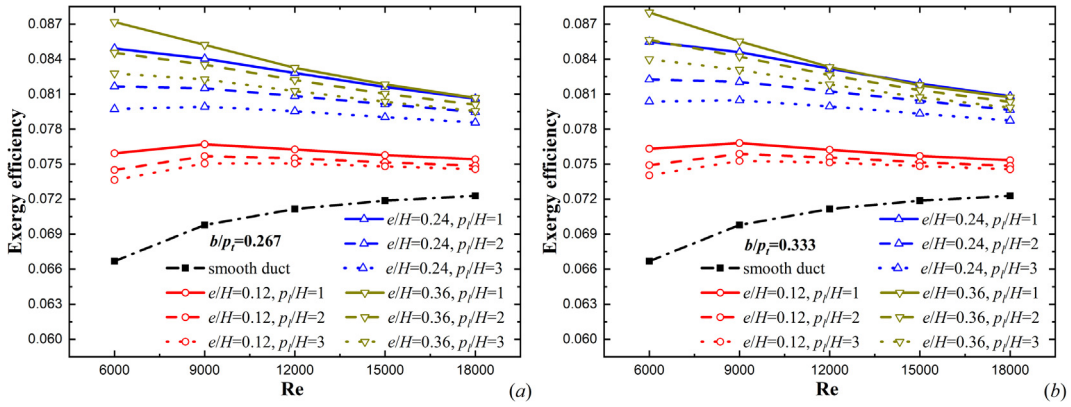

Fig. 25. The variations of exergy efficiency: (*a*) $b/p_t = 0.267$, (*b*) $b/p_t = 0.333$.

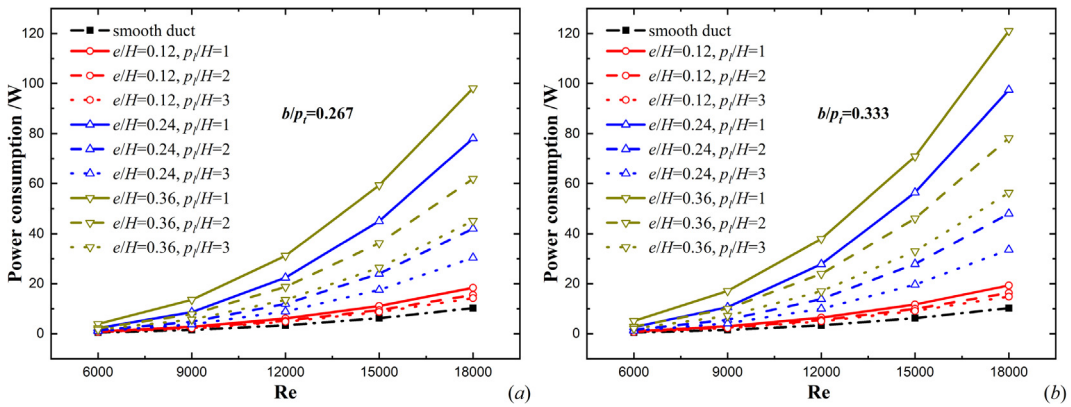

Fig. 26. The variations of power consumption: (*a*) $b/p_t = 0.267$, (*b*) $b/p_t = 0.333$.

research is moderate, while the penalty increasement in friction factor is relatively low. Fig. 28 displays the variations of energy efficiency and exergy efficiency with the increase of power consumption. The energy efficiency, exergy efficiency, and power consumption are obtained by applying the Nusselt number and friction factor to the integrated SAH introduced in the above section. As depicted in Fig. 28, both energy and exergy efficiency of present research are relatively high.

6. Conclusion

This paper proposed ITVGs to generate multi longitudinal swirls flow in the SAH. Three major conclusions were drawn as follows:

(a) In the aspect of mechanism. A pair of longitudinal swirls were found close to both sides of each ITVG. In the flow direction, the longitudinal vortex was rectangular and leaded to fully fluid mixing. The temperature distribution in the cross section was more uniform and the mean temperature of the absorber plate was dramatically decreased compared with the smooth SAH. The enhancement in convective heat transfer mainly owed to the increase of mean heat convection velocity. In the range of this paper, the upwind aligned (A1) arrangement generated the most intense longitudinal swirl flow and gave the highest thermal hydraulic performance.

(b) In the aspect of thermal hydraulic performance. The enhancement in Nusselt number was moderate, while the penalty increasement in friction factor was relatively low. The range of Nu/Nu_0, f/f_0, EEC, and R3 were 1.24–3.71, 1.39–11.8, 0.26–0.98 and 1.11–1.89, respectively. The configured parameters of $p_1/H = 1$, $e/H = 0.24$, and

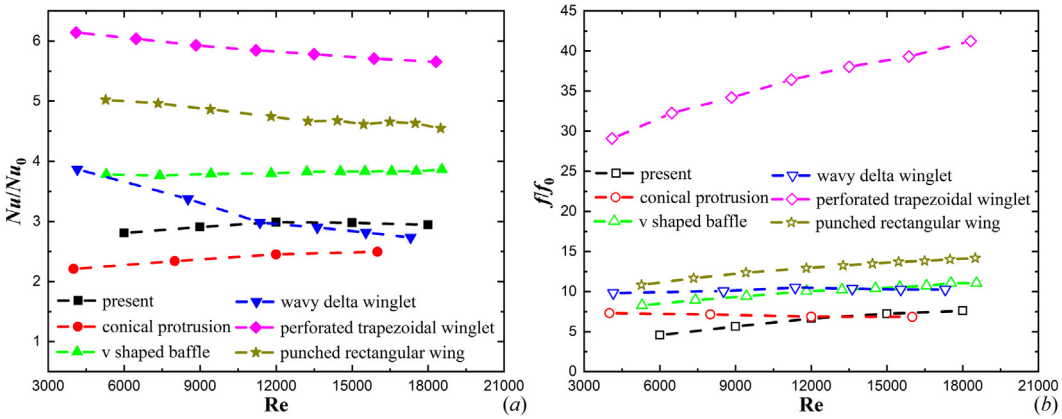

Fig. 27. Comparisons of (*a*) Nu/Nu_0 and (*b*) f/f_0 between present research and other published papers

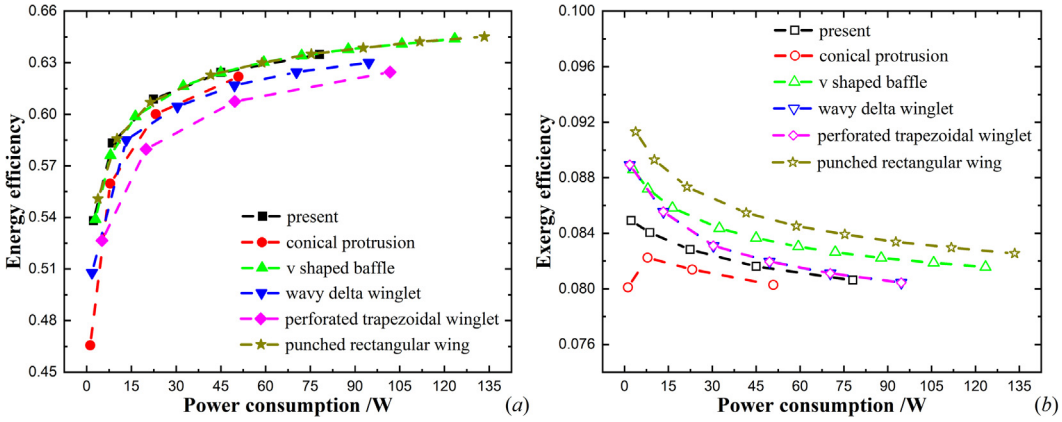

Fig. 28. Comparisons of (*a*) energy efficiency and (*b*) exergy efficiency between present research and other published papers.

$b/p_t = 0.267$ was recommended in this paper.

(c) In the aspect of efficiency analysis. In the range of this research, the energy efficiency was maximally enhanced by 24% compared with the corresponding smooth SAH. The exergy efficiency was maximally enhanced by 31% compared with the corresponding smooth SAH. Both energy and exergy efficiency of present research were relatively high compare with previous typical works.

CRediT authorship contribution statement

Hui Xiao: Conceptualization, Methodology, Software, Validation, Formal analysis, Investigation, Data curation, Writing - original draft, Writing - review & editing, Visualization. **Zhimin Dong:** Methodology, Software, Data curation. **Zhichun Liu:** Resources, Supervision, Project administration, Funding acquisition. **Wei Liu:** Resources, Supervision, Project administration, Funding acquisition.

Declaration of Competing Interest

The authors declare that they have no known competing financial interests or personal relationships that could have appeared to influence the work reported in this paper.

Acknowledgement

This work was supported by the National Natural Science Foundation of China (Grant No. 51736004).

Appendix A. Supplementary material

Supplementary data to this article can be found online at https://doi.org/10.1016/j.applthermaleng.2020.115484.

References

[1] E. Kabir, P. Kumar, S. Kumar, A.A. Adelodun, K.H. Kim, Solar energy: Potential and future prospects, Renew. Sustain. Energy Rev. 82 (2018) 894–900.
[2] F. Wang, Z. Cheng, J. Tan, Y. Yuan, Y. Shuai, L. Liu, Progress in concentrated solar power technology with parabolic trough collector system: A comprehensive review, Renew. Sustain. Energy Rev. 79 (2017) 1314–1328.
[3] M. Bhamjee, A. Nurick, D.M. Madyira, An experimentally validated mathematical and CFD model of a supply air window: Forced and natural flow, Energy Build. 57 (2013) 289–301.
[4] A.A. El-Sebaii, S.M. Shalaby, Experimental investigation of an indirect-mode forced convection solar dryer for drying thymus and mint, Energy Convers. Manage. 74 (2013) 109–116.
[5] C. Yıldırım, İ. Solmuş, A parametric study on a humidification–dehumidification (HDH) desalination unit powered by solar air and water heaters, Energy Convers. Manage. 86 (2014) 568–575.
[6] A.E. Kabeel, M.H. Hamed, Z.M. Omara, A.W. Kandeal, Solar air heaters: Design configurations, improvement methods and applications – A detailed review, Renew. Sustain. Energy Rev. 70 (2017) 1189–1206.
[7] V. Singh Bisht, A. Kumar Patil, A. Gupta, Review and performance evaluation of roughened solar air heaters, Renew. Sustain. Energy Rev. 81 (2018) 954–977.
[8] Y.L. He, W.Q. Tao, Chapter Three - Convective Heat Transfer Enhancement: Mechanisms, Techniques, and Performance Evaluation, in: E.M. Sparrow, J. Abraham, J. Gorman, Y. Cho (Eds.), Advances in Heat Transfer, vol. 46, Elsevier, 2014, pp. 87–186.
[9] H. Xiao, Z. Dong, R. Long, K. Yang, F. Yuan, A Study on the Mechanism of Convective Heat Transfer Enhancement Based on Heat Convection Velocity Analysis, Energies 12 (2019) 4175.
[10] B. Bhushan, R. Singh, Nusselt number and friction factor correlations for solar air heater duct having artificially roughened absorber plate, Sol. Energy 85 (2011) 1109–1118.
[11] P. Promvonge, T. Chompookham, S. Kwankaomeng, C. Thianpong, Enhanced heat

transfer in a triangular ribbed channel with longitudinal vortex generators, Energy Convers. Manage. 51 (2010) 1242–1249.
[12] A. Bekele, M. Mishra, S. Dutta, Performance characteristics of solar air heater with surface mounted obstacles, Energy Convers. Manage. 85 (2014) 603–611.
[13] F. Menasria, M. Zedairia, A. Moummi, Numerical study of thermohydraulic performance of solar air heater duct equipped with novel continuous rectangular baffles with high aspect ratio, Energy 133 (2017) 593–608.
[14] D. Alta, E. Bilgili, C. Ertekin, O. Yaldiz, Experimental investigation of three different solar air heaters: Energy and exergy analyses, Appl. Energy 87 (2010) 2953–2973.
[15] M.S. Manjunath, K.V. Karanth, N.Y. Sharma, Numerical investigation on heat transfer enhancement of solar air heater using sinusoidal corrugations on absorber plate, Int. J. Mech. Sci. 138–139 (2018) 219–228.
[16] T. Alam, M.-H. Kim, Heat transfer enhancement in solar air heater duct with conical protrusion roughness ribs, Appl. Therm. Eng. 126 (2017) 458–469.
[17] A.S. Yadav, J.L. Bhagoria, A CFD (computational fluid dynamics) based heat transfer and fluid flow analysis of a solar air heater provided with circular transverse wire rib roughness on the absorber plate, Energy 55 (2013) 1127–1142.
[18] K. Kumar, D.R. Prajapati, S. Samir, Heat transfer and friction factor correlations development for solar air heater duct artificially roughened with 'S' shape ribs, Exp. Therm. Fluid Sci. 82 (2017) 249–261.
[19] M.K. Sahu, R.K. Prasad, Exergy based performance evaluation of solar air heater with arc-shaped wire roughened absorber plate, Renew. Energy 96 (2016) 233–243.
[20] P. Promvonge, Heat transfer and pressure drop in a channel with multiple 60° V-baffles, Int. Commun. Heat Mass Transfer 37 (2010) 835–840.
[21] D. Jin, M. Zhang, P. Wang, S. Xu, Numerical investigation of heat transfer and fluid flow in a solar air heater duct with multi V-shaped ribs on the absorber plate, Energy 89 (2015) 178–190.
[22] J.S. Sawhney, R. Maithani, S. Chamoli, Experimental investigation of heat transfer and friction factor characteristics of solar air heater using wavy delta winglets, Appl. Therm. Eng. 117 (2017) 740–751.
[23] S. Chamoli, R. Lu, D. Xu, P. Yu, Thermal performance improvement of a solar air heater fitted with winglet vortex generators, Sol. Energy 159 (2018) 966–983.
[24] E.K. Akpinar, F. Koçyiğit, Experimental investigation of thermal performance of solar air heater having different obstacles on absorber plates, Int. Commun. Heat Mass Transfer 37 (2010) 416–421.
[25] T. Alam, M.-H. Kim, Numerical study on thermal hydraulic performance improvement in solar air heater duct with semi ellipse shaped obstacles, Energy 112 (2016) 588–598.
[26] M.S. Manjunath, K.V. Karanth, N.Y. Sharma, Numerical analysis of the influence of spherical turbulence generators on heat transfer enhancement of flat plate solar air heater, Energy 121 (2017) 616–630.
[27] A. Kumar, R.P. Saini, J.S. Saini, Experimental investigation on heat transfer and fluid flow characteristics of air flow in a rectangular duct with Multi v-shaped rib with gap roughness on the heated plate, Sol. Energy 86 (2012) 1733–1749.
[28] R.K. Ravi, R.P. Saini, Nusselt number and friction factor correlations for forced convective type counter flow solar air heater having discrete multi V shaped and staggered rib roughness on both sides of the absorber plate, Appl. Therm. Eng. 129 (2018) 735–746.
[29] S. Skullong, P. Promthaisong, P. Promvonge, C. Thianpong, M. Pimsarn, Thermal performance in solar air heater with perforated-winglet-type vortex generator, Sol. Energy 170 (2018) 1101–1117.
[30] P. Promvonge, S. Skullong, Heat transfer augmentation in solar receiver heat exchanger with hole-punched wings, Appl. Therm. Eng. 155 (2019) 59–69.
[31] J.A. Meng, X.G. Liang, Z.X. Li, Field synergy optimization and enhanced heat transfer by multi-longitudinal vortexes flow in tube, Int. J. Heat Mass Transf. 48 (2005) 3331–3337.
[32] W. Liu, P. Liu, J.B. Wang, N.B. Zheng, Z.C. Liu, Exergy destruction minimization: A principle to convective heat transfer enhancement, Int. J. Heat Mass Transf. 122 (2018) 11–21.
[33] H. Xiao, J. Wang, Z. Liu, W. Liu, Turbulent heat transfer optimization for solar air heater with variation method based on exergy destruction minimization principle, Int. J. Heat Mass Transf. 136 (2019) 1096–1105.
[34] Z.Y. Guo, W.Q. Tao, R.K. Shah, The field synergy (coordination) principle and its applications in enhancing single phase convective heat transfer, Int. J. Heat Mass Transf. 48 (2005) 1797–1807.
[35] W. Liu, P. Liu, Z.M. Dong, K. Yang, Z.C. Liu, A study on the multi-field synergy principle of convective heat and mass transfer enhancement, Int. J. Heat Mass Transf. 134 (2019) 722–734.
[36] N. Zheng, F. Yan, K. Zhang, T. Zhou, Z. Sun, A review on single-phase convective heat transfer enhancement based on multi-longitudinal vortices in heat exchanger tubes, Appl. Therm. Eng. 164 (2020) 114475.
[37] N. Zheng, P. Liu, F. Shan, J. Liu, Z. Liu, W. Liu, Numerical studies on thermo-hydraulic characteristics of laminar flow in a heat exchanger tube fitted with vortex rods, Int. J. Therm. Sci. 100 (2016) 448–456.
[38] J.A. Duffie, W.A. Beckman, Solar engineering of thermal processes, John Wiley & Sons, 2013.
[39] F. Jafarkazemi, E. Ahmadifard, Energetic and exergetic evaluation of flat plate solar collectors, Renewable Energy 56 (2013) 55–63.
[40] D. Jin, J. Zuo, S. Quan, S. Xu, H. Gao, Thermohydraulic performance of solar air heater with staggered multiple V-shaped ribs on the absorber plate, Energy 127 (2017) 68–77.
[41] ASHRAE, Standard 93–97, in: Methods of testing to determine the thermal performance of solar collectors, American Society for Heating, Refrigeration, and Air Conditioning Engineering, New York, 1977.
[42] A. Escue, J. Cui, Comparison of turbulence models in simulating swirling pipe flows, Appl. Math. Model. 34 (2010) 2840–2849.
[43] S.V.P.P.W. Deshmukh, R.P. Vedula, Heat transfer enhancement for laminar flow in tubes using curved delta wing vortex generator inserts, Appl. Therm. Eng. (2016).
[44] H. Xiao, J. Wang, Z. Liu, W. Liu, A consistent SIMPLE algorithm with extra explicit prediction — SIMPLEPC, Int. J. Heat Mass Transf. 120 (2018) 1255–1265.
[45] S.V. Patankar, Numerical HeatTransfer and Fluid Flow, Hemisphere, Washington D.C., 1980.
[46] S. Skullong, P. Promvonge, C. Thianpong, M. Pimsarn, Thermal performance in solar air heater channel with combined wavy-groove and perforated-delta wing vortex generators, Appl. Therm. Eng. 100 (2016) 611–620.